In this thesis magneto-thermoelectric effects are investigated in a systematic way to separate the transverse spin Seebeck effect from other parasitic effects like the anomalous Nernst effect. In contrast to the first studies found in the literature, in NiFe thin films a contribution of the transverse spin Seebeck effect can be excluded. This surprising outcome was crosschecked in a variety of different sample layouts and collaborations with other universities to ensure the validity of these results.

In general, this thesis solves a long time discussion about the existence of the transverse spin Seebeck effect in NiFe films and supports the importance of control measurements for the scientific community. Even if such „negative" results may not be the award winning ones, new discoveries should be treated with constructive criticism and be checked carefully by the scientific community.

Universitätsverlag Regensburg

ISBN 978-3-86845-125-2

gefördert von:

Alumni der physikalischen Fakultät der Universität Regensburg e.V.

Universität Regensburg

Maximilian Schmid

Dissertationsreihe Physik - Band 46

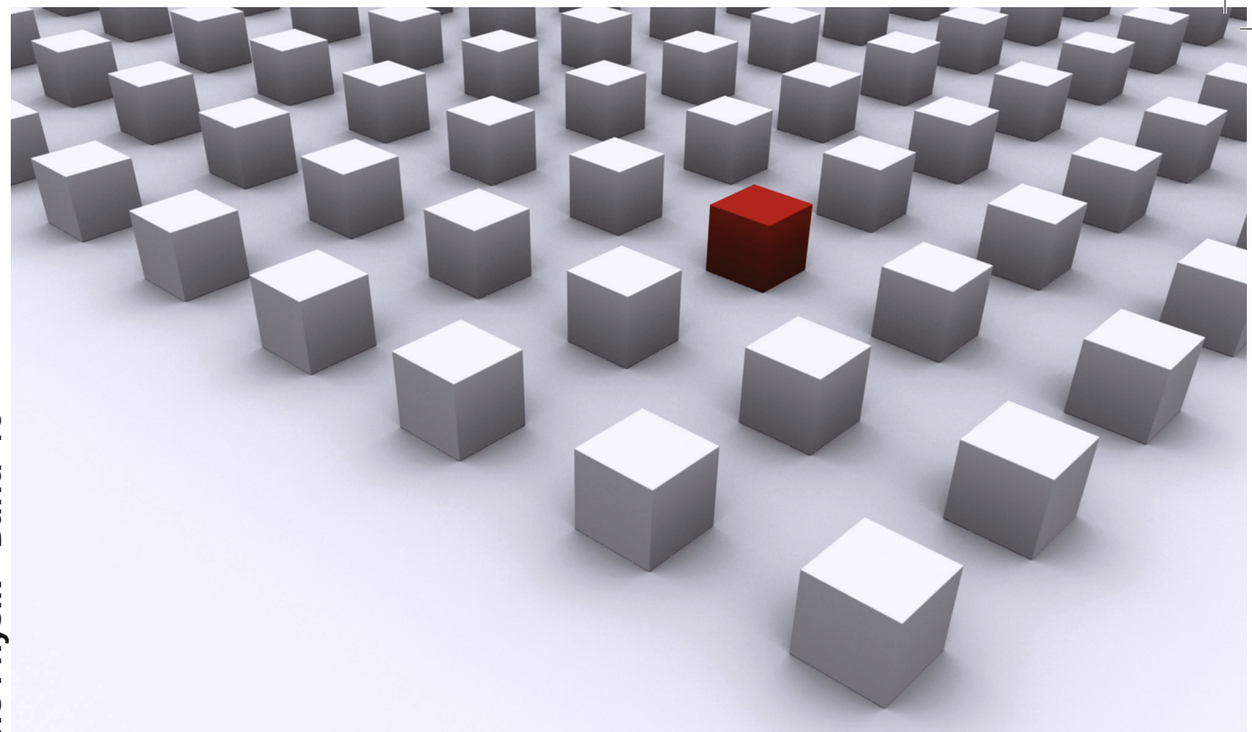

Maximilian Schmid

Magneto-thermoelectric effects in NiFe thin films

Universitätsverlag Regensburg

46 Dissertationsreihe Physik

Maximilian Schmid

Magneto-thermoelectric effects in NiFe thin films

Magneto-thermoelectric effects in NiFe thin films

Dissertation zur Erlangung des Doktorgrades der Naturwissenschaften (Dr. rer. nat.)
der Fakultät für Physik der Universität Regensburg
vorgelegt von

Maximilian Schmid

aus Erlangen

in 2014

Die Arbeit wurde von Prof. Dr. Christian Back angeleitet.
Das Promotionsgesuch wurde am 16.04.2014 eingereicht.
Das Promotionskolloquium fand am 11.12.2014 statt.

Prüfungsausschuss:
Vorsitzender: Prof. Dr. Karsten Rincke
1. Gutachter: Prof. Dr. Christian Back
2. Gutachter: Prof. Dr. Christoph Strunk
weiterer Prüfer: Prof. Dr. Ingo Morgenstern

Dissertationsreihe der Fakultät für Physik der Universität Regensburg, Band 46

Herausgegeben vom Präsidium des Alumnivereins der Physikalischen Fakultät:
Klaus Richter, Andreas Schäfer, Werner Wegscheider, Dieter Weiss

Maximilian Schmid

Magneto-thermoelectric effects in NiFe thin films

Universitätsverlag Regensburg

Bibliografische Informationen der Deutschen Bibliothek.
Die Deutsche Bibliothek verzeichnet diese Publikation
in der Deutschen Nationalbibliografie. Detailierte bibliografische Daten
sind im Internet über http://dnb.dnb.de abrufbar.

1. Auflage 2015

Leibnizstraße 13, 93055 Regensburg

Konzeption: Thomas Geiger
Umschlaggestaltung: Franz Stadler, Designcooperative Nittenau eG
Layout: Maximilian Schmid
Druck: Docupoint, Magdeburg
ISBN: 978-3-86845-125-2

Weitere Informationen zum Verlagsprogramm erhalten Sie unter:
www.univerlag-regensburg.de

Contents

1 Motivation

Since the beginning of computing there is a continuous demand for increasing computational power. In the last decades this demand could be satisfied, following an exponential growth of the computational abilities known as Moores law [1]. However, it becomes more and more challenging to satisfy this growth rate in the future. The key issue is simply Joule heating in charge based logical devices. For example, the power density of an actual CPU with 100 W TDP (Thermal Design Power) and a chip size of 2×2 cm^2 size on a 0.5 mm thick wafer is at least in the order of 500 Watt per cm^3. In comparison, the core of a nuclear power plant has an average volume power density of 50 Watt per cm^3. One attempt to reduce Joule heating is to utilize besides charge transport the spin degree of freedom of the electron. The research field, dealing with this topic, is called spintronics [2]. For example, STT-RAM (spin transfer torque random access memory) uses non-volatile TMR (tunneling magneto resistance) elements to store the data. Thus in contrast to normal charge-based RAM, there is no standby energy consumption of the devices. However, during the writing process of the single TMR elements via the STT, for a short period of time high current densities are present producing thermal gradients in the magnetic materials.

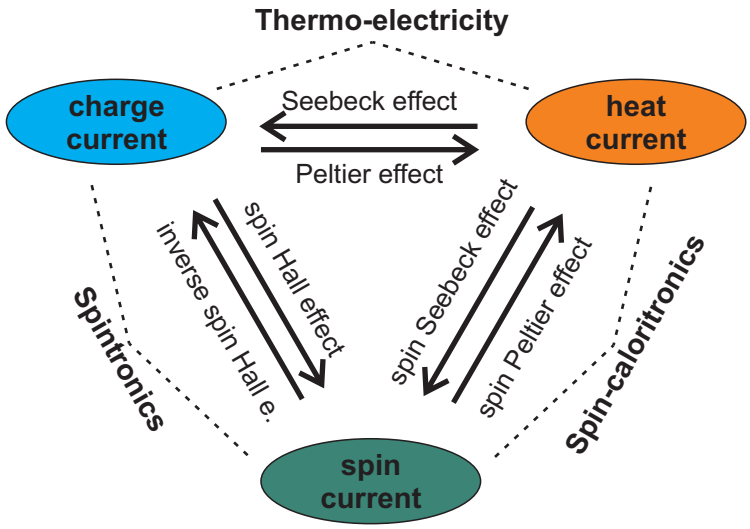

Figure 1.1: Next to Thermoelectric and Spintronic Spin-caloritronic closes the gap between heat and spin currents.

Adding logical spin operations to conventional charge based logical devices is a promising way to improve energy efficiency. Nevertheless, in this coexistence of spin and charge based logic, Joule heating will still be present and the mechanisms of the interaction between heat and spin transport is of high interest for future applications. Understanding this interaction is the aim of the new field of fundamental research called Spin-caloritronics [3]. As shown in Fig. 1.1, the interaction of charge and heat transport is well described by thermo-electricity. The interaction of charge and spin transport is part of the field of spintronics. Spin-caloritronics now closes the gap between spin and heat transport. Inspired by this new way of influencing the spin system by heat currents, new effects like thermal spin injection [4] [5], thermal spin transfer torque [6], the spin Seebeck effect [7] and the spin Peltier effect [8] are under investigation. All have in common that a non-equilibrium thermal distribution manipulates the spin distribution. However, spin transport can proceed in different ways. It can be charge-based (e.g. thermal spin injection) or charge-independent (spin Seebeck effect in insulators).

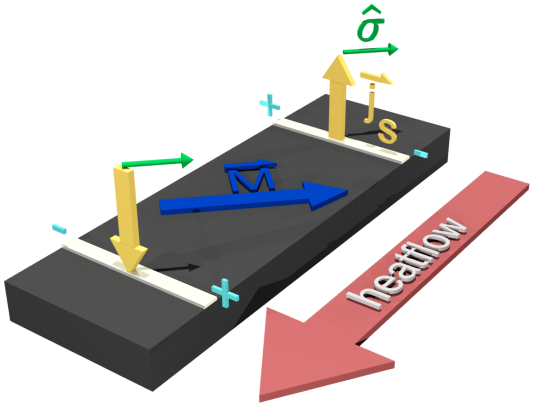

Figure 1.2: Schematic overview of the transverse spin Seebeck effect. An in-plane temperature gradient in an in-plane magnetized ferromagnetic system leads to a laterally varying spin imbalance and to a spin current $\vec{j}_S$ entering an attached detector strip. The polarization $\vec{\sigma}$ of $\vec{j}_S$ is parallel to the magnetization $\vec{M}$. Due to the inverse spin Hall effect, the spin current is converted to an electro-motive force which builds up a voltage signal at the ends of the detector strip (indicated by $+$ and $-$). One key feature of the transverse spin Seebeck effect is a sign change of $\vec{j}_S$ when moving the detector strip from the hot to the cold side of the sample.

In this work, the focus is set on the Spin Seebeck effect in the transverse configuration (TSSE) in NiFe thin films, like used in the first observation by Uchida et al. in 2008 [7]. As seen in Fig. 1.2, in case of TSSE, a thermal gradient is supposed to be the driving force for a lateral varying spin imbalance along the ferromagnetic layer. In order to transform this spin signal into a directly accessible voltage signal, a spin sink, i.e. a Pt detector strip, is attached to the ferromagnetic layer.

The inverse spin Hall effect then converts the spin current entering the detector strip into a voltage signal, which is picked up at the ends of the strip. However, when performing TSSE measurements, further magneto-thermoelectric effects, e.g. the Nernst-Ettingshausen effect, have to be considered as well. In order to be able to separate these additional voltages, which do not originate from the TSSE, but can mask the TSSE contribution, a systematic study is needed. In this study different substrate materials and sample layouts are investigated for various temperature profiles. By including finite element simulations and numerical calculations it is possible to assign the different contributions and to draw conclusions about the TSSE in NiFe thin films.

The first part of this thesis describes the interaction of spin and charge currents in general and provides information on magneto-thermoelectric effects which may be present in the TSSE configuration. A short overview of the observations on the SSE made so far and the theory behind the SSE is provided afterwards. The experimental part describes the setups and samples used for this work. By means of a typical dataset, key features as well as the analysis of the measured data are explained. The following experimental results show the essential measurements, simulations and calculations which made it possible to separate known magneto-thermoelectric effects from a possible TSSE contribution. In the last part the results are compared to the observations of the TSSE in NiFe films of other groups.

2 Theory

2.1 The interaction of charge and spin currents

2.1.1 The drift diffusion approach

An electron's spin is coupled to its motion via the spin orbit interaction (SOI). In single atoms this interaction leads to spin splitting of the energy levels and can explain parts of the fine structures of spectral lines of atoms. In solids SOI influences the spin dependent band structure and plays an important role in spin dependent transport phenomena. In this section, the focus will be on the interaction of charge currents with spin currents in nonmagnetic materials. Let us first define the ordinary charge current $\vec{j}$ and spin current $\boldsymbol{Q}$ without any spin orbit interaction, following the drift diffusion model of Dyakonov [9]. $\vec{j}$ is the vector of the charge current density with direction $\hat{j}$ and magnitude $|\vec{j}|$. In the drift diffusion model then

$$\frac{\vec{j}}{-e} = -\mu n\vec{E} - D\vec{\nabla}n, \tag{2.1}$$

with the charge carrier mobility μ , the diffusion coefficient D, the electric field $\vec{E}$ and the electron concentration n. By contrast, the spin current cannot be written as a simple vector, since it has not only a direction $\hat{j}_S$ and magnitude $|\vec{j}_S|$, but also a polarization $\hat{\sigma}$ it carries along $\hat{j}_S$. So the spin current can be described by a tensor

$$\boldsymbol{Q} = \begin{pmatrix} Q_{xx} & Q_{xy} & Q_{xz} \\ Q_{yx} & Q_{yy} & Q_{yz} \\ Q_{zx} & Q_{zy} & Q_{zz} \end{pmatrix}, \tag{2.2}$$

where the first index describes the spatial direction of the spin current ($\hat{j}_S$) and (Q_{ix}, Q_{iy}, Q_{iz}) its magnitude ($|\vec{j}_S|$) and its polarization direction $\hat{\sigma}$. The components of $\boldsymbol{Q}$ are given by the drift diffusion equation for the spin current carried by spin polarized electrons

$$\frac{Q_{ij}}{\hbar/2} = -\mu E_i S_j - D\frac{\partial S_j}{\partial x_i}, \tag{2.3}$$

with $\vec{S}$ being the spin polarization density vector. So far, equations (2.1) and (2.3) do not include SOI. When including this interaction, the two currents/equations are coupled in the following way:

$$j_i = j_i^{(o)} - \frac{2e}{\hbar}\gamma\epsilon_{ijk}Q_{jk}, \tag{2.4}$$

$$Q_{ij} = Q_{ij}^{(o)} + \frac{\hbar}{2e}\gamma\epsilon_{ijk}j_k, \tag{2.5}$$

where $j_i^{(o)}$, $Q_{ij}^{(o)}$ are the charge and spin current without SOI, ϵ_{ijk} is the Levi-Civita symbol (the Einstein notation is used) and γ the coupling parameter [9]. Equation (2.4) and (2.5) show that due to spin orbit interaction, a non polarized charge current can produce a spin current and vice versa. Further following Dyakonov, they can be transformed to

$$\vec{j} = \mu en\vec{E} + eD\vec{\nabla}n + e\gamma\mu\vec{E}\times\vec{S} + e\gamma D\vec{\nabla}\times\vec{S}, \tag{2.6}$$

$$Q_{ij} = -\frac{\hbar}{2}\mu n E_i S_j - \frac{\hbar}{2}D\frac{\partial S_j}{\partial x_i} + \epsilon_{ijk}\left(\frac{\hbar}{2}\gamma\mu n E_k + \frac{\hbar}{2}\gamma D\frac{\partial n}{\partial x_k}\right). \tag{2.7}$$

The new terms of equation (2.6) and (2.7) can be linked to several SOI effects. In the following, we will relate to the $e\gamma D\vec{\nabla}\times\vec{S}$ term known as the inverse spin Hall effect (ISHE) and the $\epsilon_{ijk}\left(\frac{\hbar}{2}\gamma\mu n E_k + \frac{\hbar}{2}\gamma D\frac{\partial n}{\partial x_k}\right)$ term known as the spin Hall effect (SHE). Later on, we also will have a short view on the anomalous Hall effect (ANE) described by the $e\gamma\mu\vec{E}\times\vec{S}$ term. For further discussion please see [9].

2.1.2 The spin Hall effect

As shown above, in the presence of SOI theory predicts spin dependent scattering of the conduction electrons in a normal metal or a doped semiconductor leading to a spin separation perpendicular to the electron flow, the so called spin Hall effect (SHE) [10,11]. At first, spin orbit mediated scattering mechanisms were proposed as the origin of this effect [10–12]. In addition to these extrinsic components [13] dominated by skew scattering [14] and side jump scattering [15], also an intrinsic part which originates from the band structure itself was suggested [16,17]. Up to

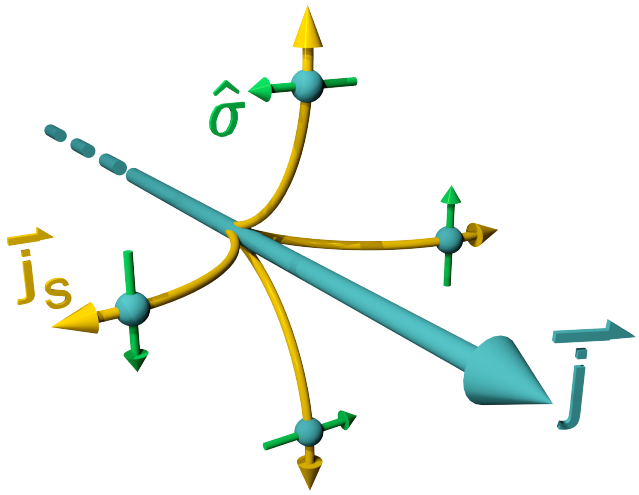

Figure 2.1: Scheme of the spin Hall effect. An unpolarized charge current $\vec{j}$ produces spin currents $\vec{j_S}$ perpendicular to $\vec{j}$. The polarization $\hat{\sigma}$ of $\vec{j_S}$ is perpendicular to both, $\vec{j}$ and $\vec{j_S}$.

now, the relative ratio of these effects is still under discussion. Notwithstanding the theoretical disagreement on the origins of this effect, it can be measured in various materials [18–22].

As sketched in Fig. 2.1, different spin orientations are deflected in different directions perpendicular to the unpolarized current $\vec{j}$. Due to the analogy to the ordinary Hall effect, this effect was called the spin Hall effect [11]. To be more precise, we use the spin current tensor $\boldsymbol{Q}$ which contains the information about the direction of the spin current $\hat{j}_S$, its magnitude $\left|\vec{j}_S\right|$ and its polarization $\hat{\sigma}$. To obtain the spin current along a certain direction $\hat{j}_S$, one multiplies its transposed vector $\hat{j}_S^{\mathrm{T}}$ with $\boldsymbol{Q}$:

$$\left|\vec{j}_S\right| \hat{\sigma} = \hat{j}_S^{\mathrm{T}} \cdot \boldsymbol{Q} \tag{2.8}$$

The resulting vector displays the polarization direction $\hat{\sigma}$ times the magnitude of the spin current $\left|\vec{j}_S\right|$ flowing along $\hat{j}_S$.

Neglecting any other source of spin currents, assuming a bulk normal metal and introducing the dimensionless spin Hall angle θ_{SH} as a coupling parameter between the charge current and the produced spin current, the matrix elements can be written as:

$$Q_{ij} = -\frac{\hbar}{2e}\theta_{\mathrm{SH}}\epsilon_{ijk}j_k \tag{2.9}$$

which is identical with the second term of equation (2.5). The factor $-\frac{\hbar}{2e}$ connects the charge transport ($-e$ per second) to the spin transport ($\hbar/2$ per second). Here it has to be mentioned that in some publications these quantities are already included in $\vec{j}$ and $\vec{j}_S$.

As an example, we start with a charge current $\vec{j}$ along the y-axis.

$$\vec{j} = \begin{pmatrix}0\\1\\0\end{pmatrix}\left[\frac{\mathrm{A}}{\mathrm{m}^2}\right] \tag{2.10}$$

The resulting spin current tensor then is:

$$\boldsymbol{Q} = 1.05\cdot 10^{-34}\theta_{\mathrm{SH}}\begin{pmatrix}0 & 0 & -1\\0 & 0 & 0\\1 & 0 & 0\end{pmatrix}\left[\frac{\mathrm{J}}{\mathrm{m}^2}\right] \tag{2.11}$$

displaying the following resulting spin currents along the principal axes:

$$\begin{aligned}
&\hat{j}_S = \pm\hat{x}; \quad \left|\vec{j}_S\right| = 1.05\cdot 10^{-34}\theta_{\mathrm{SH}}\left[\tfrac{\mathrm{J}}{\mathrm{m}^2}\right]; \quad \hat{\sigma} = \mp\hat{z};\\
&\hat{j}_S = \pm\hat{y}; \quad \left|\vec{j}_S\right| = 0; \qquad\qquad\qquad\quad \hat{\sigma} = 0;\\
&\hat{j}_S = \pm\hat{z}; \quad \left|\vec{j}_S\right| = 1.05\cdot 10^{-34}\theta_{\mathrm{SH}}\left[\tfrac{\mathrm{J}}{\mathrm{m}^2}\right]; \quad \hat{\sigma} = \pm\hat{x};
\end{aligned} \tag{2.12}$$

As sketched in Fig. 2.1, the charge current in y-direction leads to pure spin currents in the x-z-plane. Since opposite directions carry the same charge but opposite polarization, the net charge current is zero.

2.1.3 The inverse spin Hall effect

Apart from the spin Hall effect (SHE) another effect was predicted [10, 11]: the inverse spin Hall effect (ISHE) as the reciprocal process to the SHE. A pure spin current is converted into a charge current as sketched in Fig. 2.2. The generated charge current $\vec{j}_{\mathrm{ISHE}}$ can be written as

$$\vec{j}_{\mathrm{ISHE}} = \theta_{\mathrm{ISHE}}\vec{j}_S \times \hat{\sigma} \tag{2.13}$$

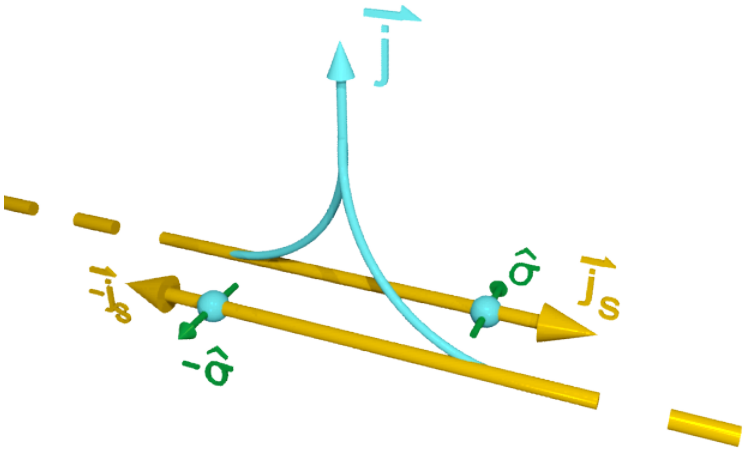

Figure 2.2: Scheme of the inverse spin Hall effect. A pure spin current (displayed by the two charge based spin currents $\vec{j}_S$ and -$\vec{j}_S$ with opposite polarization $\hat{\sigma}$ and $-\hat{\sigma}$) produces an unpolarized charge current $\vec{j}$ perpendicular to $\vec{j}_S$ and its polarization $\hat{\sigma}$.

with θ_{ISHE} as the ISHE coefficient [23]. Using the spin current tensor $\boldsymbol{Q}$ from section 2.1.2, equation (2.13) can also be written as

$$\vec{j}_{\mathrm{ISHE}} = \theta_{\mathrm{ISHE}} Q_{ij} \epsilon_{ijk} \hat{e}_k = \theta_{\mathrm{ISHE}} (\boldsymbol{Q}_{(row=k)})^{\dagger} \times \hat{e}_k \tag{2.14}$$

with the unity base vectors $\hat{e}_k$. In order to evaluate θ_{ISHE} one can compare equation (2.9) and (2.14) leading to:

$$\theta_{\mathrm{ISHE}} = -\frac{2e}{\hbar} \theta_{\mathrm{SH}} \tag{2.15}$$

As an example, we take a pure spin current $\vec{j}_S$ along the z-axis. In detail this can be viewed as a charge current with a polarization along the x-axis running along the z-axis and a charge current with opposite polarization running along the opposite direction (see Fig. 2.2). Thus, the charge currents cancel out and one obtains a pure spin current with the spin current tensor

$$\boldsymbol{Q} = 1.05 \cdot 10^{-34} \begin{pmatrix} 0 & 0 & 0 \\ 0 & 0 & 0 \\ 1 & 0 & 0 \end{pmatrix} \left[\frac{\mathrm{J}}{\mathrm{m}^2} \right] \tag{2.16}$$

and the charge current results from equation (2.14):

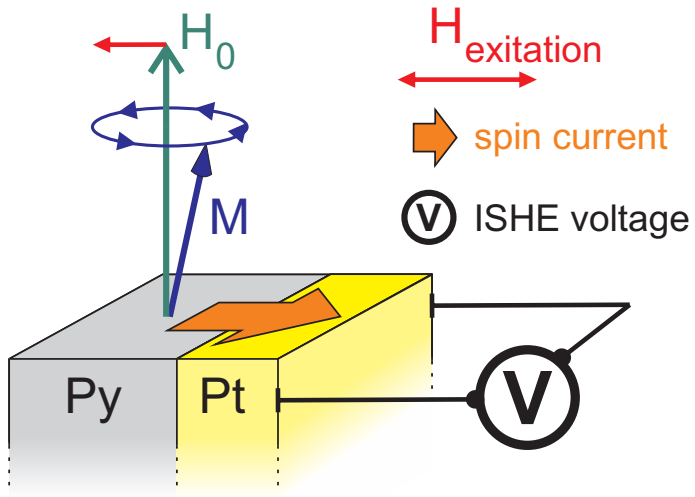

Figure 2.3: Sketch of a spin pumping measurement technique. The oscillating magnetization pumps a spin current into the Pt layer. This spin current is then measured via the ISHE.

$$\vec{j}_{\mathrm{ISHE}} = \theta_{\mathrm{SH}} \begin{pmatrix} 0 \\ +1 \\ 0 \end{pmatrix} \left[\frac{\mathrm{A}}{\mathrm{m}^2}\right] \tag{2.17}$$

In this simple case, also equation (2.13) shows immediately the resulting charge current $\vec{j}$ in y-direction. For simplicity and without any loss of generality, in the following we will display a pure spin current with one arrow. In the case of charged based spin transport, this can be seen as the sum of two spin polarized currents running in opposite direction and carrying opposite polarization like sketched in Fig. 2.2.

2.1.4 The spin Hall angle

In a few words I would like to explain why there is so little consensus about the measured spin hall angles so far. As there is no way to measure a spin current directly, the conversion of the spin current into a measurable quantity is needed. In case of the spin hall effect, the spin current can produce a spin accumulation at the edges of the material. By adding a ferromagnet (FM) to the normal metal (NM), a part of the spin current can be transmitted into the ferromagnet and influence the damping of the magnetization precession via the spin transfer torque [24]. The other way round, a ferromagnet's oscillating magnetization can 'pump' a spin current into the NM as shown in Fig. 2.3. This spin current then

θ_{SH}	Reference
0.0037^{a}	Kimura et al. [22]
0.012^{b} (± 0.002)	Feng et al. [25]
0.013^{b} (± 0.002)	Mosendz et al. [29]
0.076^{c} ($0.056 < \theta_{SH} < 0.16$)	Liu et al. [24]
0.08^{b} (± 0.01)	Azevedo et al. [26]
0.12^{b} (± 0.04)	Obstbaum et al. [27]

Table 2.1: Spin Hall angle θ_{SH} measured by different groups using ^{a}non local lateral spin valves, ^{b}spin pumping and ^{c}spin torque measurements.

produces a measurable voltage signal due to the ISHE [25–27]. The third way is to measure a non local voltage in lateral spin valve structures using the NM as a spin sink or a spin current source [22]. However, in all of these cases the spin mixing conductance of the interface/interfaces and the spin transport properties in the NM need to be known exactly so that the spin hall angle can be extracted from these measurements. For example, we take spin pumping measurements where microwaves are used to excite the magnetization and the corresponding inverse spin Hall effect voltage is measured in an attached NM layer. There,

$$\theta_{SH} \propto \frac{V_{ISHE}\, c_{NM}\, t_{NM}}{\lambda_{SD}\, g_{\uparrow\downarrow}\, \tanh(\frac{t_{NM}}{2\lambda_{SD}})} \tag{2.18}$$

with c_{NM} the conductivity, t_{NM} the thickness and λ_{SD} the spin diffusion length of the NM as well as $g_{\uparrow\downarrow}$ the spin mixing conductance of the FM/NM interface [27]. Equation 2.18 shows that variations of the single parameters sum up to a big uncertainty in the spin Hall angle. Table 2.1 shows θ_{SH} of Pt measured by different groups and with different measurement techniques. θ_{SH} shows a broad scatter of at least one order of magnitude. Especially the different values of λ_{SD}, ranging from 1.4 nm [24] to 7 nm [28] for Pt, support this divergence.

2.2 Nernst-Ettingshausen effects

2.2.1 From the Hall to the Nernst-Ettingshausen effect

When applying a charge current $\vec{j}$ and a magnetic field $\vec{H}$ perpendicular to $\vec{j}$ in a conducting material, an electric field $\vec{E}$ perpendicular to both occurs [30]. This is the well known Hall effect named after Edwin Hall:

$$\vec{E} = R_{\mathrm{H}}\vec{j} \times \mu_0\vec{H} \tag{2.19}$$

with the Hall coefficient R_{H} as a material parameter. In the 19th century Walther Nernst and Albert von Ettingshausen found an effect, where an applied temperature gradient $\vec{\nabla}T$ in contribution with a magnetic field $\vec{H}$ applied perpendicular to $\vec{\nabla}T$ produces an electro-motive force perpendicular to both [31]. This is the so called Nernst-Ettingshausen effect or simply the Nernst effect.

$$\vec{E} = \alpha\vec{\nabla}T \times \mu_0\vec{H}, \tag{2.20}$$

with the Nernst coefficient α as a material parameter. While Nernst and Ettingshausen at first did not show a direct relation to the Hall effect, the two effects have the same microscopic origin. Regarding the Hall effect, the charge carriers carrying the current $\vec{j}$ are affected by the Lorentz force and build up the perpendicular electric field. By contrast, in the case of the Nernst effect, there is no current $\vec{j}$ so that, at first sight, the Lorentz force cannot be the origin of the electric field. Nevertheless, the applied temperature gradient $\vec{\nabla}T$ builds up an electro-motive force $\vec{E}_{\mathrm{emf}} = -S\vec{\nabla}T$ with the Seebeck coefficient S due to the common Seebeck effect. In a simple picture, this force can be seen as a dynamic equilibrium where constantly hot charge carriers $\vec{j}_{\mathrm{hot}}$ above the Fermi level flow along $\vec{\nabla}T$ and are compensated by a back flow of cold electrons $\vec{j}_{\mathrm{cold}}$ below the Fermi level. These currents are affected by the Hall effect and produce Hall voltages opposite to each other. These Hall voltages are of different magnitude - even since the net charge current $\vec{j}_{\mathrm{hot}} - \vec{j}_{\mathrm{cold}} = 0$ - since the hot electrons have different group velocities than the cold ones (assuming a simple Fermi distribution). Thus, the Nernst effect is the difference of these two Hall voltages. In reality, there exist not only two channels, one for the hot and one for the cold electrons, but many possible channels depending on the band structure of the material and the thermal distribution of the charge carriers. The sum over all these channels then gives the resulting transverse electric field. Nevertheless, using the above model, when changing from Hall to Nernst effects, $\vec{j}$ can be substituted with $\vec{\nabla}T$ while using the associated coefficients. This substitution is going to be used in the following to connect the magneto-electric to the magneto-thermoelectric effects.

2.2.2 The anomalous Nernst effect

In addition to the ordinary Hall and Nernst effects, in ferromagnets an additional spin orbit coupling term has to be included, the so called anomalous Hall

effect (AHE) and anomalous Nernst effect (ANE) as the associated magneto-thermoelectric effect:

$$\vec{E} = R_{\mathrm{AHE}} \vec{j} \times \hat{m} \tag{2.21}$$

$$\vec{E} = \alpha_{\mathrm{ANE}} \vec{\nabla} T \times \hat{m} \tag{2.22}$$

with $\hat{m}$ the unity vector of the magnetization $\vec{M}$, R_{AHE} the anomalous Hall effect coefficient and α_{ANE} the anomalous Nernst effect coefficient. While their magnitude usually exceeds the ones of the ordinary effects, the origin of these anomalous effects remained unknown for long time [9]. As described in section 2.1.1, the effect originates from spin orbit coupling phenomena in the FM. But its exact microscopic origin and the magnitude of an intrinsic and extrinsic contribution are still under discussion [32, 33].

$$\alpha_{\mathrm{ANE}} = \alpha_{\mathrm{ANE}}^{\mathrm{intrinsic}} + \alpha_{\mathrm{ANE}}^{\mathrm{skew}} + \alpha_{\mathrm{ANE}}^{\mathrm{sidejump}} \tag{2.23}$$

However, in the state-of-the-art picture, a superposition of impurity scattering (skew scattering and side jump) and an intrinsic contribution are in good agreement to experimental data [33,34] despite the ongoing debate about their ratio.

2.3 The anisotropic magneto-thermoelectric power

2.3.1 The anisotropic magneto-thermoelectric power as the thermal analog to the anisotropic magneto resistance

In a ferromagnetic material, the resistance depends on the direction of the magnetization $\hat{m}$ with respect to $\vec{j}$ [35]. Thus, it cannot be seen as a scalar, but shows an anisotropy concerning the magnetization direction in the ferromagnet and can be written as a tensor.

$$\rho = \begin{pmatrix} \rho_{xx} & \rho_{xy} & \rho_{xz} \\ \rho_{yx} & \rho_{yy} & \rho_{yz} \\ \rho_{zx} & \rho_{zy} & \rho_{zz} \end{pmatrix} \tag{2.24}$$

This effect is called the anisotropic magneto resistance (AMR). Due to SOI, the resistance of the ferromagnet depends on the direction of the applied current with

respect to the magnetization alignment. The difference in resistance between the current running perpendicular or parallel to the magnetization direction leads to the well known $\cos^2\vartheta$ dependence of the resistance. Here ϑ denotes the angle of magnetization with respect to the applied current. Introducing $\rho_\perp$ and $\rho_\parallel$ as the resistances for $\vartheta = 90°, 270°$ and $\vartheta = 0°, 180°$, one receives for a current $\vec{j}$ applied to a ferromagnet as the expression for the electric field $\vec{E}$:

$$\vec{E} = \rho_\perp \left[\vec{j} - \left(\hat{m}\cdot\vec{j}\right)\cdot\hat{m}\right] + \rho_\parallel \left(\hat{m}\cdot\vec{j}\right)\cdot\hat{m} + R_{\mathrm{AHE}}\hat{m}\times\vec{j}, \tag{2.25}$$

where $\hat{m}$ denotes the unity vector of the magnetization $\vec{M}$. Excluding the last term - the AHE contribution - equation 2.25 simplifies to

$$\vec{E} = \rho_\perp\vec{j} + \left(\rho_\parallel - \rho_\perp\right)\left(\hat{m}\cdot\vec{j}\right)\cdot\hat{m} \tag{2.26}$$

Similar to the substitution used for changing from Hall to Nernst effects, we substitute $\vec{j}$ with $\vec{\nabla}T$ and $\rho_{\parallel,\perp}$ are exchanged by the Seebeck coefficients $S_{\parallel,\perp}$. Thus, equation 2.26 transforms to:

$$\vec{E} = S_\perp\vec{\nabla}T + \left(S_\parallel - S_\perp\right)\left(\hat{m}\cdot\vec{\nabla}T\right)\cdot\hat{m} \tag{2.27}$$

Using the Seebeck tensor $\boldsymbol{S}$, the electric field $\vec{E}$ can also be expressed by:

$$\begin{pmatrix}E_x\\E_y\\E_z\end{pmatrix} = \begin{pmatrix}S_{xx} & S_{xy} & S_{xz}\\S_{yx} & S_{yy} & S_{yz}\\S_{zx} & S_{zy} & S_{zz}\end{pmatrix}\cdot\begin{pmatrix}\nabla T_x\\\nabla T_y\\\nabla T_z\end{pmatrix} \tag{2.28}$$

In order to evaluate the matrix elements $S_{i,j}$ in a way that relates to our experimental quantities, we express $\hat{m} = \sin\varphi\cos\vartheta\hat{x} + \sin\varphi\sin\vartheta\hat{y} + \cos\varphi\hat{z}$ and $\vec{\nabla}T = \nabla T_x\hat{x} + \nabla T_y\hat{y} + \nabla T_z\hat{z}$, where $\hat{x}$,$\hat{y}$,$\hat{z}$ are the unity vectors along the principle axes, ϑ the angle of $\hat{m}$ in the x-y-plane with respect to the -x-axis and φ the angle of $\hat{m}$ with respect to the z-axis. Using these expressions and equation 2.27 and 2.28, the Seebeck tensor can be written as:

$$S = (S_\parallel - S_\perp)\begin{pmatrix}\sin^2\varphi\cos^2\vartheta & -\sin^2\varphi\sin\vartheta\cos\vartheta & -\sin\varphi\cos\varphi\cos\vartheta\\-\sin^2\varphi\cos\vartheta\sin\vartheta & \sin^2\varphi\sin^2\vartheta & \cos\varphi\sin\varphi\sin\vartheta\\-\sin\varphi\cos\varphi\cos\vartheta & \cos\varphi\sin\varphi\sin\vartheta & \cos^2\varphi\end{pmatrix} + S_\perp\mathbb{1} \tag{2.29}$$

Equation 2.27 and 2.29 describe the thermal analogue to the AMR. Since it belongs to the magneto-thermoelectric effects and since the thermoelectric power

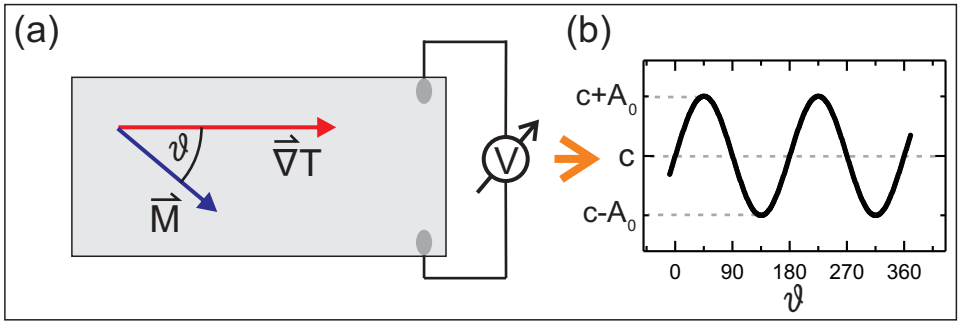

Figure 2.4: (a) Measurement geometry for the transversal AMTEP with the magnetization $\vec{M}$ in the x-y-plane, $\vec{\nabla}T$ along the x-axis and ϑ the angle of $\vec{M}$ with respect to the -x-axis. (b) Angle dependence of the measured transversal voltage. A_0 denotes the signal amplitude, c displays a random offset voltage.

(TEP) is a well known expression, we call this effect the anisotropic magneto-thermoelectric power or short the AMTEP.

2.3.2 Planar Nernst effect or the transverse anisotropic magneto-thermoelectric power

In a normal AMR measurement using the 4-point-technique, a current $\vec{j}$ is driven through an in-plane magnetized ferromagnet and the voltage is measured along the direction of $\vec{j}$. However, if the voltage is probed perpendicular to the current $\vec{j}$, a voltage signal

$$V_y \propto \sin\vartheta\cos\vartheta \tag{2.30}$$

can be measured (resulting from Eq. 2.26) [36]. This effect was somewhat misleadingly called the planar Hall effect since an in-plane magnetization and an in-plane current generate an in-plane voltage. However, the effect originates from the spin orbit interaction in the ferromagnet and is the transversal component of the AMR so that it is more useful to call it the transversal AMR.

Again, there is a thermal analogue to this effect: The so called planar Nernst effect [37] or transverse AMTEP. Let us use equation 2.28 and 2.29 and assume a voltage measurement along the y-direction, so that only E_y contributes to the signal and therefore only three of the nine matrix elements are important for the further discussion:

$$E_y = \begin{pmatrix} S_{yx} & S_{yy} & S_{yz} \end{pmatrix} \cdot \begin{pmatrix} \nabla T_x \\ \nabla T_y \\ \nabla T_z \end{pmatrix} \tag{2.31}$$

Moreover, assuming the temperature gradient is applied along the x-axis and the magnetization lies in the x-y-plane ($\varphi = 90°$), as sketched in Fig. 2.4(a), equation 2.31 simplifies to

$$E_y = S_{yx} \cdot \nabla T_x = -(S_{\parallel} - S_{\perp}) \nabla T_x \sin\vartheta \cos\vartheta \tag{2.32}$$

the planar Nernst effect. In order to be consistent with the transverse AMR mentioned above, this effect is going to be called the transverse component of the AMTEP (or short the AMTEP). It should be pointed out that the angular dependence of E_y (respectively V_y), sketched in Fig. 2.4(b), has a maximum amplitude A_0 at angles of $\vartheta = 45°$ and $\vartheta = 135°$.

2.4 The spin Seebeck effect

Apart from the magneto-thermoelectric effects mentioned in the previous sections, the spin Seebeck effect (SSE) was discovered in 2008 by Uchida et al. [7]. There, a temperature gradient produces a spin current in a ferromagnetic material. This spin current is then transformed to a measurable voltage using the inverse spin Hall effect in a NM attached to the ferromagnet. Since the first observation the research field of spin caloritronics has attracted a lot of attention and the existence of the SSE was published in a variety of materials [38–44]. Nevertheless, origin and quantity of this effect are still heavily under discussion. Especially parasitic effects obscuring the clear observation of the spin Seebeck effect are one major point of this discussion [40, 45]. In the following sections we first concentrate on the observations of the Spin Seebeck effect made so far and then provide an overview of the evolution of the theoretical explanation. Finally, we will discuss some critical points.

2.4.1 The transverse spin Seebeck effect

In 2008, Uchida et al. [7] published for the first time the existence of the spin Seebeck effect in a transverse geometry as sketched in Fig. 2.5. A temperature gradient $\vec{\nabla} T$ was applied in the plane of a Permalloy layer and a voltage was measured at the ends of a Pt strip attached to the Py layer perpendicular to the temperature gradient. It was supposed that a spin current $\vec{j_S}$ flows along $\vec{\nabla} T$ and is converted to a voltage signal in the Pt strip utilizing the ISHE. To be more precise, $\vec{j_S}$ carries a polarization $\vec{\sigma}$ parallel to the magnetization vector of the ferromagnetic layer $\vec{M}$ along $\vec{\nabla} T$ applied in x-direction. This spin current then enters (perpendicular to the sample plane along the z-axis) the Pt detector

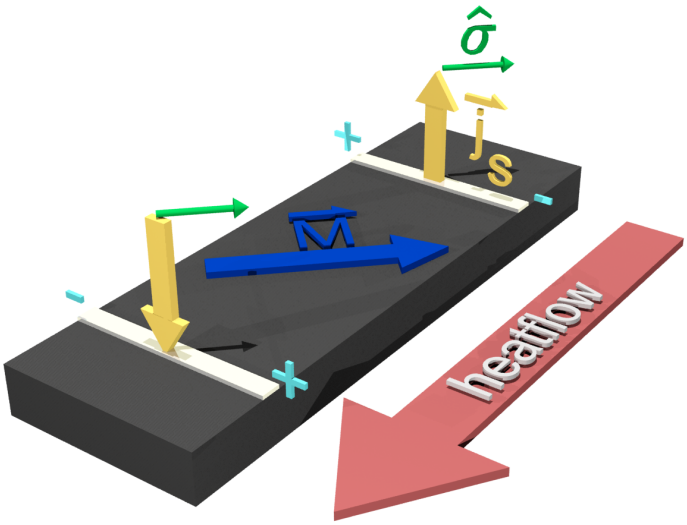

Figure 2.5: Schematic overview of the TSSE. An in-plane temperature gradient in an in-plane magnetized ferromagnetic system leads to a lateral varying spin imbalance and to a spin current $\vec{j}_S$ entering an attached NM detector strip. The polarization $\vec{\sigma}$ of $\vec{j}_S$ is parallel to the magnetization $\vec{M}$. Due to the ISHE the spin current is converted to an electro motive force which builds up a voltage signal at the ends of the detector strip (indicated by + and −). One key feature of the TSSE is a sign change of $\vec{j}_S$ when moving the detector strip from the hot to the cold side of the sample.

strip and transforms to an electric field in y-direction following the equation of the ISHE:

$$\vec{E}_{\mathrm{ISHE}} = \theta_{\mathrm{ISHE}} \vec{j}_S \times \hat{\sigma} \tag{2.33}$$

This electric field builds up an electrical voltage V_y picked up at the ends of the Pt strip. One of the key features of the TSSE is the change of polarity of V_y when moving the strip from the hot to the cold side of the sample and a vanishing signal exactly in the middle between both sides. Besides this lateral dependence, V_y scales linearly with the temperature difference ΔT. To prove that the observed signals are related to the spin current entering the Pt strip, Uchida et al. performed measurements without the Pt strip directly on the Py and found no signal [7]. Additionally, the angular dependence on the external magnetic field follows a cosine dependence in good agreement with equation 2.33. After the discovery of the TSSE in Py on Al_2O_3 the effect has been observed in Fe, Ni, NiFe layers on MgO and Al_2O_3 substrates [38]. Next to the metallic materials the TSSE is also observable in insulating ferromagnets. Uchida et al. observed all main features of the TSSE in a YIG layer on a GGG substrate leaving an open question of the role of the conduction electrons [39].

In the meantime, Jaworski et al. performed measurements with the diluted magnetic semiconductor GaMnAs and made, at first sight, similar observations: A changing signal when moving from hot to cold side and the same angle dependencies as Uchida et al. where detected. Nevertheless, in their experiments the signal was still observable without the Pt detector strip which, as they claim, is related to a higher spin orbit coupling in the GaMnAs itself [40]. One new point observed on GaMnAs was the conservation of the signal when introducing gaps in the ferromagnetic layer. The authors suggested an important role of the phonons in the substrate which, in their case, was GaAs. The observation of an Umklapp-peak at low temperatures supports their suggestions.

2.4.2 The longitudinal spin Seebeck effect

Besides the original configuration with an in-plane temperature gradient, measurements have been performed in FM/NM bilayers with a temperature gradient applied out-of-plane as sketched in Fig. 2.6. This more simple layout is called the longitudinal configuration. It was first measured in a Pt/YIG bilayer on a GGG substrate. There Uchida et al. observed a voltage signal proportional to the applied temperature gradient [43]. Furthermore the signal vanishes when changing the alignment of the external magnetic field from perpendicular to parallel to the voltage measurement as expected from equation 2.33. Next to YIG the LSSE has been measured in several other materials [41–44]. However, the LSSE is restricted to insulating materials since the configuration of $\vec{\nabla}T$ perpendicular to $\vec{M}$ comes along with the anomalous Nernst effect which in conductors is obscuring the measured LSSE signals.

2.4.3 Evolution of theory

After this overview of the observation of the SSE in different configurations and materials we now focus on the theoretical description of the SSE. In the first work about the TSSE in Py films by Uchida et al. [7] the authors suggested that the spin dependent chemical potentials $\mu_{\uparrow,\downarrow}$ have different dependencies on the temperature, so that in general $\mu_\uparrow(T) \neq \mu_\downarrow(T)$. Furthermore, since the SSE is vanishing in the middle of the sample, $\mu_\uparrow = \mu_\downarrow$ at this point and the chemical potentials look like two crossing lines with the crossing point in the middle of the sample as sketched in Fig. 2.7(a). Thus, when applying a temperature gradient to the ferromagnet, a spin imbalance is generated and diffuses into the Pt detector strip. This model had to be neglected since the spin diffusion length of Py is in the range of a few nm and a spin current could only generate a spin imbalance within a few nm to the edge of the sample and not along the mm scaled sample like used in [7].

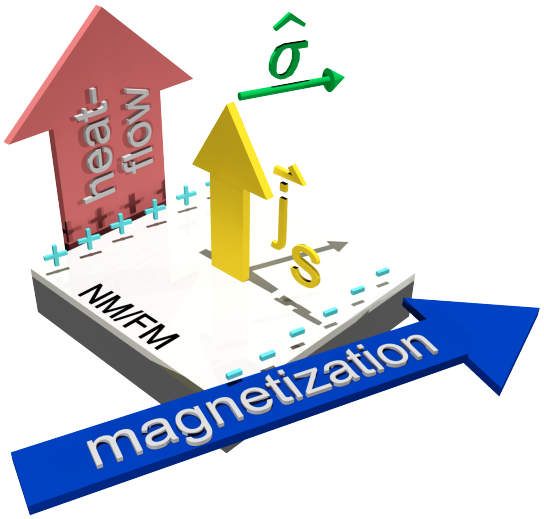

Figure 2.6: Schematic overview of the LSSE. An out-of-plane temperature gradient in an in-plane magnetized ferromagnetic layer leads to an out-of-plane spin current $\vec{j}_S$ entering an attached NM layer. The polarization $\vec{\sigma}$ of $\vec{j}_S$ is parallel to the magnetization. Due to the ISHE the spin current is converted to an electro motive force which builds up a voltage signal in the NM layer (indicated by + and −).

The observation of the SSE in the ferromagnetic insulator YIG lead to a new theory of the SSE in insulators as a magnon driven effect. Xiao et al. suggested a three temperature model including the magnon, phonon and electron temperature [46]. The spin current entering the detector strip originates from a temperature imbalance of the magnon temperature in the ferromagnet in comparison to the electron temperature in the detector strip at the interface between both. This imbalance then leads to a spin current into the detector strip. The model fits the experiments for Pt on YIG but fails for metallic systems like Pt on Py. Thus, at first glance, there were two models: one for metallic and one for insulating ferromagnetic systems. But there was a lack of a united theory.

After the observations of Jaworski et al. [40] that a gap in the ferromagnetic layer does not divide the system into two separate parts with hot and cold side but leaves the observations similar to a closed ferromagnetic layer, the substrate has to be taken into account. The only possibility to explain the remaining lateral position information with a discontinuous ferromagnetic layer is to take the phonons of the substrate into account. The similarity of temperature dependence of the TSSE signal at low temperatures to the phonon Umklapp-peak supports the idea of a phonon contribution [47, 48]. Adachi et al. [47] finally included a phonon magnon drag contribution to the model of the magnon mediated SSE by Xiao et al. [46]. Fig. 2.7(b) shows the latest theoretical explanation of the TSSE [47]. The phonons carry the heat along the temperature gradient in the

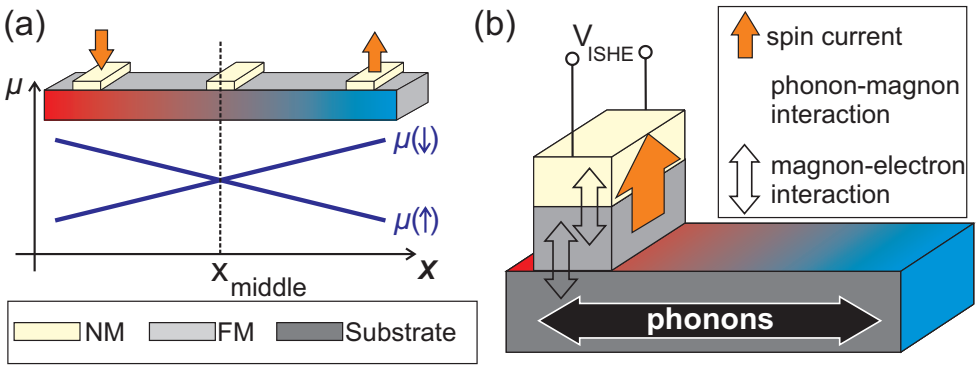

Figure 2.7: (a) Sketch of the first theoretical explanation of Uchida et al. with temperature dependent chemical potentials $\mu(\uparrow)$,$\mu(\downarrow)$ [7]. (b) Sketch of the latest theoretical picture by Adachi et al. including the substrate phonons [47].

substrate. These phonons then interact with the magnons in the ferromagnetic layer and a spin current flows across the FM/NM interface into the NM described by the magnon mediated SSE [46]. Later on, Uchida et al. observed acoustic spin pumping which shows that a phonon imbalance in the substrate can produce a spin current across a FM/NM interface [49].

2.4.4 Spin Seebeck effect under discussion

Like in any new research field spin-caloritronics is constantly under evolution which includs critical voices and some setbacks. As described above, the theoretical explanation of the SSE has changed a few times and may not yet have reached the final state. Alongside the theoretical evolution some problems and setbacks occurred on the experimental side. After the first enthusiasm on the observation of the spin Seebeck effect, no one was able to reproduce the measurements with Pt/Py. Thus the transverse spin Seebeck effect in metallic systems has so far only been investigated by one research group in Japan. Even some samples showing the SSE in Japan did not show any signal in other laboratories [50]. Furthermore, by investigating the transverse voltage signals in a more detailed way, some other contributions masking the transverse voltage signal turned out to be very hard to separate from the spin Seebeck effect. These are namely the anomalous Nernst effect and the AMTEP. Since the AMTEP is always present in the transverse configuration, small SSE signals may hide behind this effect. But as the angular dependence of the AMTEP is different to the one of the SSE, the signals may be separated from each other. In contrast, the ANE does not contribute in a perfectly transverse configuration where $\vec{\nabla}T$ and $\vec{M}$ are in the sample plane. However, small disturbances like an out-of-plane component of $\vec{\nabla}T$ or $\vec{M}$ can lead to a contribution to the voltage signal with the same angular

dependence as the spin Seebeck effect. Therefore, to separate the ANE and the SSE is a challenging task [40, 45]. Up to now there is no consensus about the existence and the magnitude of the TSSE in metallic systems.

When using insulating ferromagnets, the AMTEP and the ANE can be excluded at first glance and the signals can be attributed directly to the SSE. Thus at least the longitudinal spin Seebeck effect seems to be quite solid and could be reproduced by other groups [41, 44]. However there is still one open question: When attaching Pt to a ferromagnetic insulator, e.g. YIG, there may be an induced magnetization in the first monolayers of the Pt (called the proximity effect). This would lead to an ANE signal as $\vec{\nabla}T$ is perpendicular to $\vec{M}$ and the signals could not be attributed directly to the SSE. X-ray magnetic circular dichroism (XMCD) spectroscopy measurements have been performed by different groups and it seems that the proximity effect is depending on the growth conditions of the Pt layer [51, 52]. This point is still under discussion.

2.4.5 The role of the out-of-plane temperature gradient

As described above, the TSSE setup, using metallic ferromagnetic layers, is very sensitive to an out-of-plane temperature gradient $(\vec{\nabla}T)_z$. As an example, we estimate $(\vec{\nabla}T)_z$ which is sufficient to give rise to a transverse voltage signal in the order of 1 µV for a standard Py sample as used in [7](width: $d = 4\,\mathrm{mm}$). We obtain:

$$V_y = d\alpha_{\mathrm{ANE}}(\vec{\nabla}T)_z \cos\theta, \tag{2.34}$$

with ϑ being the angle between the magnetization and the -x-axis. Using $\alpha_{\mathrm{ANE}} = 2.6\,\mu\mathrm{V/K}$ for Py [45] a temperature gradient of $(\vec{\nabla}T)_z = 100\,\mathrm{K/m}$ is sufficient to give a voltage amplitude of about 1 µV. Thus, a temperature difference of 1 µK in a 20 nm thick Py layer can sophisticate the TSSE in the µV range. Taking this high sensitivity into account, the appearance of an out-of-plane temperature gradient needs to be investigated carefully when performing TSSE measurements. One often discussed suggestion is to match the thermal conductivities of the substrate and the ferromagnetic layer. As sketched in Fig. 2.8, a mismatch of the thermal conductivities results at least in a finite temperature difference between the substrate and the FM layer when applying an in-plane temperature gradient. In reality, this temperature difference across the interface may introduce a finite $(\vec{\nabla}T)_z$ in the ferromagnetic layer. However, the thermal conductivities of very thin layers may differ from in-plane to out-of-plane and furthermore both may be different from the bulk values in the literature, which is why it is hard to match substrate and layer. Nevertheless, Al_2O_3 and MgO seem to be suitable substrates

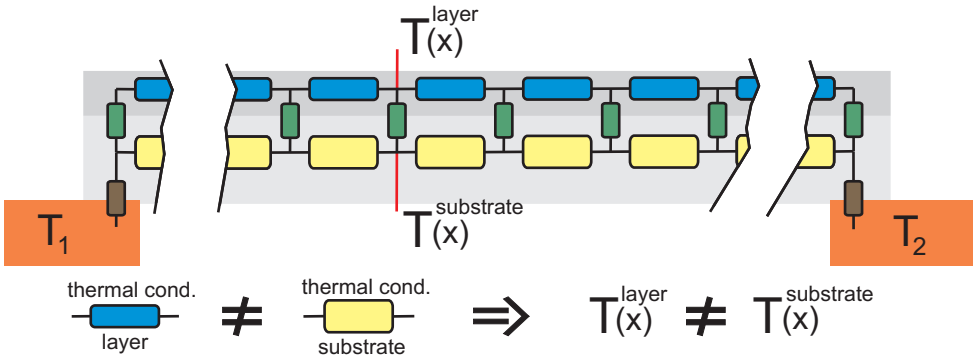

Figure 2.8: Schematic picture of a TSSE sample connected to a heat reservoir at both ends ($T_1 \neq T_2$). The resistor network shows the electrical analog of the heat transport alongue the sample. A mismatch of the thermal conductivities leads to a temperature difference between substrate and ferromagnetic layer.

for Py, Ni and Fe at room temperature as demonstrated in [7,38]. Since the ANE is restricted to conducting ferromagnetic materials, the TSSE in insulators is not affected by it. However, it might be possible that the TSSE in insulators is an artifact of an out-of-plane temperature gradient, which itself then produces a LSSE signal at the location of the detector strip [53].

3 Experiment

3.1 Setup 1 for bulk Py films

In order to measure the TSSE, the requirements to the setup are at first glance to produce a stable temperature gradient $\vec{\nabla}T$, to apply a magnetic field $\vec{H}$ and to measure the low voltage signals. Furthermore, in order to investigate the TSSE in a systematic way it should be possible to change the temperature gradients and to vary the base temperature of the system. Additionally, while planning the setup one wants it to be open for further modification, since the field of spin caloritronics is under constant evolution. Thus, the setup is built up in a modular way. For the supply of the temperature gradient we decided to use Peltier elements mounted on a single heat sink connected to a flow cryostat. This enables the system to operate in a broad temperature range. Since the Peltier elements may not work sufficiently well at low temperature, the sample holder carrying the sample and the Peltier elements is designed to be removable so that it can be changed to a low temperature version. This modification also allows to mount the sample outside of the setup and to have easy access to the holder itself. To minimize the influences of convection and to isolate the inner part from the surrounding, the cryostat is mounted in a vacuum chamber. Finally, a pair of Helmholtz coils supplies a rather homogeneous magnetic field at the sample location and is mounted around the vacuum chamber. In the following we concentrate on the main parts of the setup which are the sample holder and the vacuum chamber.

3.1.1 Sample holder

The inner core of the setup consists of the head of the cryostat and the attached sample holder. This holder carries the two Peltier elements, the thermal sensors and all electrical connections for these devices. As shown in Fig. 3.1, the holder has a base plate including the electrical connections. On top of this plate two Cu blocks, adjustable in distance, carry two Peltier elements. In order to ensure a homogeneous temperature profile on the top of the Peltier elements, two Cu pads are glued to the top. These Cu pads are also thermally connected to the Pt-100 sensors which are used for the temperature control. To this level, all connections

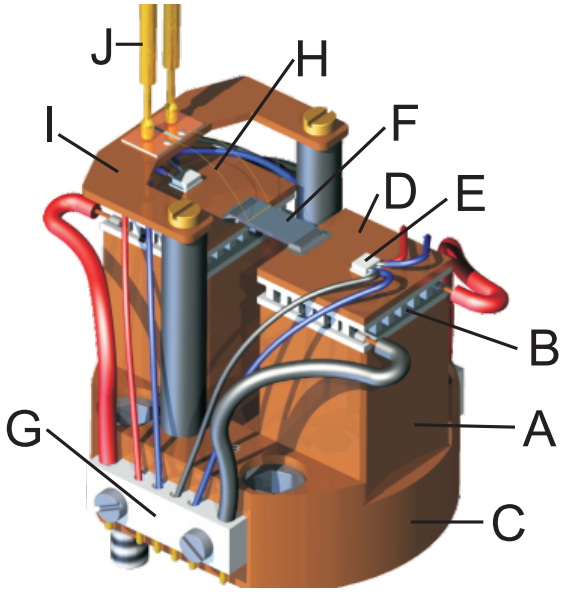

Figure 3.1: Inner part of the setup. Two Cu blocks (A), carrying the Peltier elements (B), are attached to a common base plate (C). Two Cu-pads (D) are attached to the top of the Peltier elements ensuring a homogeneous temperature profile. The Pt 100 sensors (E) and the sample (F) are glued onto the Cu-pads with conducting silver paste. The Peltier elements and the Pt 100 sensors are electrically supplied from the bottom (G) while the voltage measuring lines (H) run to a copper bridge (I). The signal is picked up by two spring contacts (J).

are provided by the base plate and run to the bottom of the cryostat. In order to ensure a minimal influence of these supply wires to the measuring signal, the voltage measuring lines run to the top of the setup. With this lateral separation a decoupling of the voltage measurement to the temperature control is provided. In detail, the Au bond wires coming from the sample are glued to a 0.2 mm thick ceramic circuit board soldered onto a thermally isolated Cu bridge. This bridge ensures a homogeneous temperature profile of the contact area and reduces Seebeck voltages originating from different contact temperatures. Finally, this signal is picked up by two gold spring probes and is fed through the top of the chamber.

3.1.2 Vacuum chamber

The vacuum chamber fulfills three main tasks: It prevents convection, isolates the cryostat from the surrounding and shields the inner parts electrically from the surrounding. The chamber consists of two parts: a 10 mm thick walled Aluminum tube carrying the cryostat and a removable Aluminum cap. The system is pumped via the cryostat and a base pressure of 10^{-6} mbar can be reached. In

order to ensure easy access for the cooling line from the Nitrogen/Helium reservoir into the cryostat the chamber is lifted up by an Aluminum frame. At the chamber all feed-throughs except for the voltage measuring lines are implemented in the bottom part of the cryostat, separating the Peltier elements from the temperature measurement. As described above, the voltage signal is picked up by two spring probes. These probes provide contact to a circuit board (in the first version) carrying a preamplifier or simply contact to the feed-throughs. Thus, the cap provides access to the sample holder and contacts the Cu bridge for the low voltage measurements. The thick walled Aluminum chamber ensures a homogeneous temperature profile and buffers - due to its heat capacity - fluctuations in the surrounding temperature. Around the chamber a rotatable table carries a pair of Helmholtz coils. Finally, the top of the setup is housed in an Aluminum cage, which is designed to shield the setup further from the surrounding.

3.2 Setup 2 for suspended Py layers

For the investigation of the suspended Py films on SiN_x membranes we use a different setup (Setup 2). The samples (as will be explained in section 3.3.2) already include the heater and bond pads for electrical connections so that there is no need to supply a temperature gradient from the sides of the setup. Due to this reason and due to the size of the samples we decided to measure the samples in an already existing cryo system which is designed for magneto-resistance measurements. It delivers an insulation vacuum of at least 10^{-6} mbar as well as stable temperature conditions. Furthermore, it shares the same measuring geometry as the bulk setup (also see Fig. 3.4).

3.3 Samples

For a better overview, in this section the samples used in this thesis are categorized. In principle, two main types of samples have been used: There are the Py films deposited on MgO and GaAs bulk substrates and the suspended Py layers grown on SiN_x membranes as shown in the following.

3.3.1 Py films on bulk substrates

The samples on bulk substrates used in this thesis are partly produced at the University of Regensburg in a sputtering/evaporation system and partly supplied by Daniel Meier from the University of Bielefeld. Both setups operate at a base

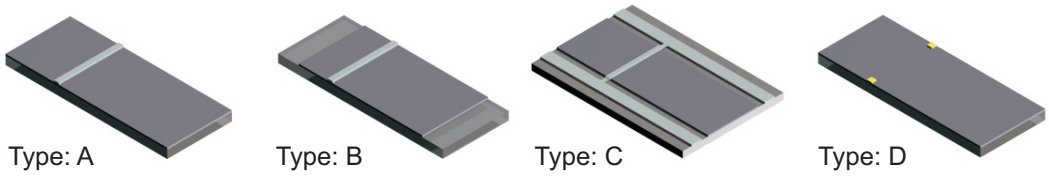

Figure 3.2: Overview of the different sample types and layouts used in Setup 1.

pressure of 10^{-8} mbar and provide the shadow mask sputtering technique. All measurements are done at four main types of samples displayed in Fig. 3.2. All of them share the Py layer but can differ in size, substrate and detector material.

In the following, the samples will be referred to these different types:

- Type A: A 20 nm thick Py layer is evaporated on a 10 mm × 4 mm and 0.5 mm thick MgO substrate. Without breaking the vacuum, a 100 µm wide and 10 nm thick Pt or Cu strip is deposited on the Py layer. The strip is located about 3mm away from one edge.

- Type B: Similar to Type A, but the Py layer was sputtered through a shadow mask and covers an area of 7.5 mm × 4 mm of the MgO substrate.

- Type C: A 20 nm thick and 4 mm wide Py layer is deposited onto a 12 mm × 8 mm and 0.6 mm thick intrinsic GaAs substrate. Without breaking the vacuum, a 20 nm thick and 100 µm wide Pt strip, including two Pt contact lines, is sputter deposited on top through a shadow mask. This creates the possibility to contact the Pt strip at one end of the sample and thus to neglect any influence of the contact wires to the temperature profile of the sample.

- Type D: As a reference sample, we use a sample of Type A without the Pt detector strip. On the pure Py layer, two Au contact pads of about 100 µm × 100 µm are structured using a Ti adhesion layer.

Before mounting the samples to the sample holder, two 50 µm Au bond wires are glued to the ends of the detector strip / pads with electrically conducting silver epoxy and a contact area of about 100 µm × 200 µm. After checking the contacts the sample is glued to the Cu pads with conducting silver paste as shown in Fig. 3.1.

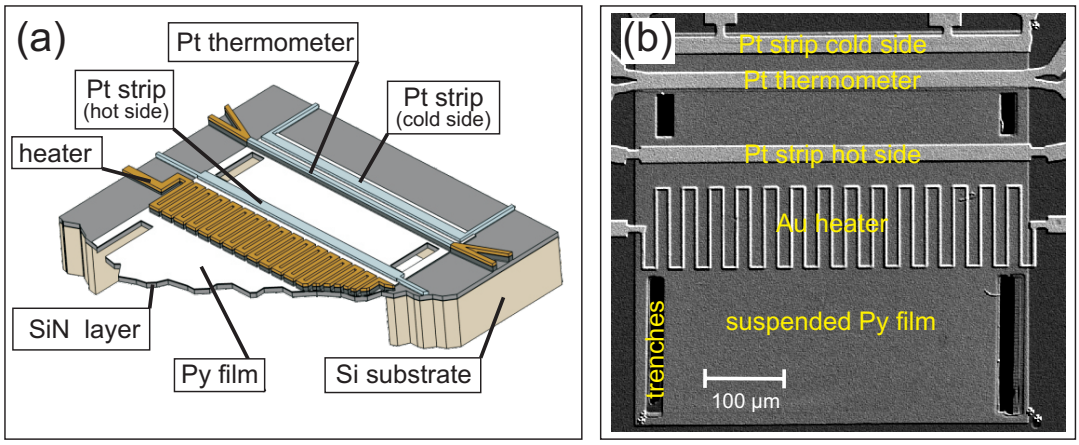

Figure 3.3: (a) Scheme of the suspended Py layers on SiN_x membranes. The membrane carries two Pt detector strips, one close to the heater, the other one close to the heat bath, as well as an Au heater meander and a Pt thermometer. The Au heater and the Pt thermometer are electrically isolated from the Py layer. (b) SEM picture of the suspended Py layer on a $500 \times 500\,\mu m^2$ SiN_x membrane.

3.3.2 Py films on SiN_x membranes

The suspended Py films on SiN_x membranes have been produced by Sasmita Srichandan at the University of Regensburg. Fig. 3.3 illustrates the sample design and shows a SEM picture obtained from one of the samples. We use $500\,\mu m \times 500\,\mu m$ large and 100 nm thick SiN_x membranes on Si substrates. On top of these, 20 nm of Py and 10 nm of Pt are deposited by sputtering in-situ at a base pressure of 10^{-8} mbar. Then, two 20 µm wide Pt strips are structured by removing the maintaining Pt layer by Ar etching. Contacts to these Pt detector strips are produced by a subsequent e-beam lithography step. Then, an Au meandering heater wire as well as two Pt thermometers are structured on top of the Py layer. The heater and the Pt thermometers are electrically isolated from the Py film using a 30 nm thick Al_2O_3 insulating layer which is deposited in an atomic layer deposition (ALD) process. Finally, the regions of the membrane located at the sides have been milled away using focused ion beam (FIB) etching in order to thermally isolate the device from the heat sink and to provide a homogeneous temperature gradient between the heater and the heat sink.

3.4 Measurement and data processing

In the following, the measuring process as well as the processing of the measured data is going to be described. At the end, some key features of the experimental data will be explained.

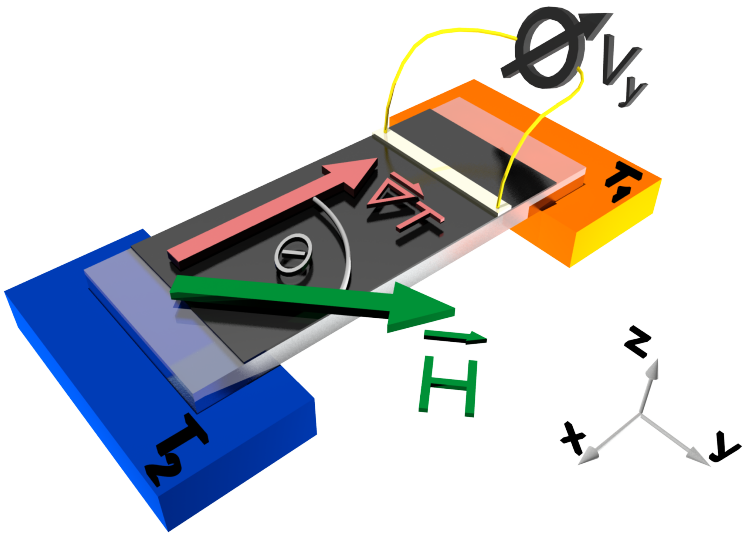

Figure 3.4: Sketch of the measurement geometry. The temperature gradient is applied along the x-axis and can be varied in magnitude and sign. The magnetic field can be swept from -4.5 mT to 4.5 mT at various angles of θ with respect to the -x-axis. The voltage is probed along the y-axis.

3.4.1 Measurement and geometry

The basic method in SSE measurements is to apply a thermal gradient along the sample and to record the voltage while sweeping the magnetic field. Fig. 3.4 displays the orientations in our setup. The temperature gradient $\vec{\nabla}T$ is always applied in the x-direction but can be reversed. The voltage V_y is probed along the y direction at the ends of the detector strip. x_{strip} denotes the distance between the detector strip and the heat reservoir T_1. The magnetic field is swept from -4.5 mT to +4.5 mT at various angles θ with respect to the -x-axis. The sweep steps are set to 0.05 mT and averaged to 0.1 mT. In practice, an integration time of about 1 s per data point and averaging over 8 magnetic sweeps per angle θ turned out to be the best parameters for high signal to noise ratio and low drift. In a standard dataset, θ is rotated in steps of 30° which is the best compromise between angle resolution and measurement time. With these parameters, one dataset consumes about 12 hours of measuring time and can be performed over night with most stable conditions.

Fig. 3.5 shows a typical dataset for a temperature difference of 50 K between the two Cu pads. The strip of the type B sample is located at the hot side and the temperatures of the Peltier elements have been set to T_1= 343 K and T_2= 293 K. The sweeps range from -4.5 mT to 4.5 mT and θ is rotated in steps of 30°. The dataset shows three main features. The distinct peak dip structure of

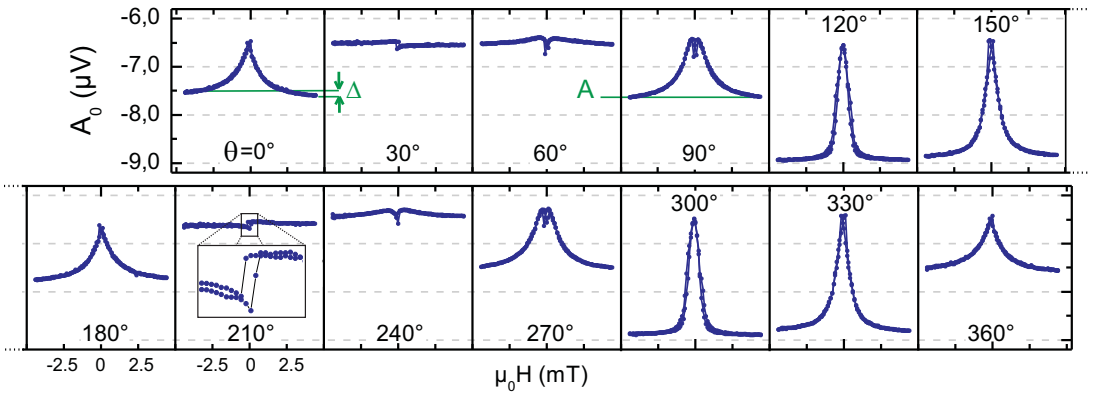

Figure 3.5: Transverse voltage V_y vs. magnetic field and angle θ. $-4.5\,\mathrm{mT} \leq \mu_0 H \leq 4.5\,\mathrm{mT}$, T_1=343 K and T_2=293 K. The noise level in each sweep is 10 nV. Sample type B (Pt/Py/MgO), $x_{\mathrm{strip}} = 1\,\mathrm{mm}$.

the single voltage traces around $\mu_0 H \approx 0\,\mathrm{mT}$ and an oscillation of the baseline (saturation values) with a period of 180°. Besides these two dominant parts, a small difference near the saturation values for the positive $\mu_0 H > 0\,\mathrm{mT}$ and the negative $\mu_0 H < 0\,\mathrm{mT}$ branch of the voltage traces is observed.

3.4.2 Data processing

In order to separate the above contributions to the signal, the sweeps are divided into three parts:
The negative branch near saturation with $\mu_0 H \leq -4\,\mathrm{mT}$.
The positive branch near saturation with $\mu_0 H \geq 4\,\mathrm{mT}$.
And the middle part with $-4\,\mathrm{mT} \geq \mu_0 H \leq 4\,\mathrm{mT}$.
For now, we neglect the middle part and concentrate on the left and right branches. At first, we average over the two branches and obtain:

$$V_- = \langle V_y(\mu_0 H \leq -4\,\mathrm{mT}) \rangle \tag{3.1}$$

$$V_+ = \langle V_y(\mu_0 H \geq 4\,\mathrm{mT}) \rangle \tag{3.2}$$

In order to get a measure of the base line, we calculate

$$A = \frac{1}{2}(V_- + V_+) \tag{3.3}$$

and for the difference we take

$$\Delta = V_- - V_+ \tag{3.4}$$

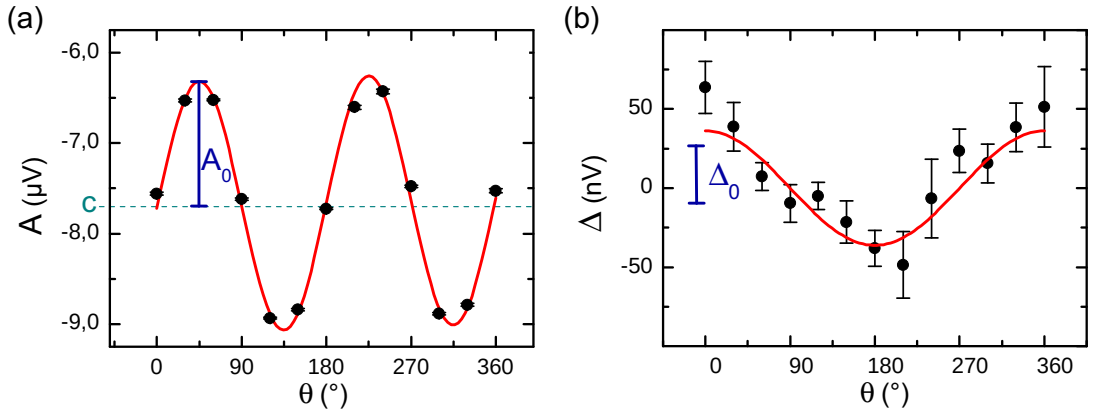

Figure 3.6: (a) A vs. θ. The red line shows the $2A_0 \sin\theta\cos\theta + c$ fit. (b) Δ vs. θ. The red line shows the $\Delta_0 \cos\theta$ fit; Sample type B (Pt/Py/MgO), $x_{strip} = 1\,\mathrm{mm}$.

By performing these steps for each angle θ we obtain $A(\theta)$ and $\Delta(\theta)$ as shown in Fig. 3.6. The error bars display the statistical error of the averaging process. As discussed in section 2.3.1, the above geometry matches the configuration of the AMTEP. Since the AMTEP is symmetric with respect to the applied magnetic field, its contribution is restricted to the average signal A and absent in the difference Δ. The expected functional dependence $A(\theta)$ originating from the AMTEP is:

$$A(\theta) = 2A_0 \sin\theta\cos\theta \tag{3.5}$$

with A_0 as the oscillation amplitude. Taking into account that all constant contributions, like the ordinary Seebeck effect or any other offset of V_y, directly contribute to A, we include an offset constant c:

$$A(\theta) = 2A_0 \sin\theta\cos\theta + c \tag{3.6}$$

Fig. 3.6(a) shows a fit of equation 3.6 to the experimental data. Since the data points perfectly agree with the prediction of the AMTEP and the $\sin\theta\cos\theta$ dependence is uniquely connected to the AMTEP, the oscillation of $A(\theta)$ can be purely related to this effect. Concerning $\Delta(\theta)$ we choose a

$$\Delta(\theta) = \Delta_0 \cos\theta \tag{3.7}$$

fit function (see Fig. 3.6(b)), with $\Delta_0 = (36 \pm 6)\,\mathrm{nV}$ as the oscillation amplitude. This function is motivated by the expected $\cos\theta$ dependence of the TSSE and the ANE. The validation of this choice and a detailed discussion on $\Delta(\theta)$ is given

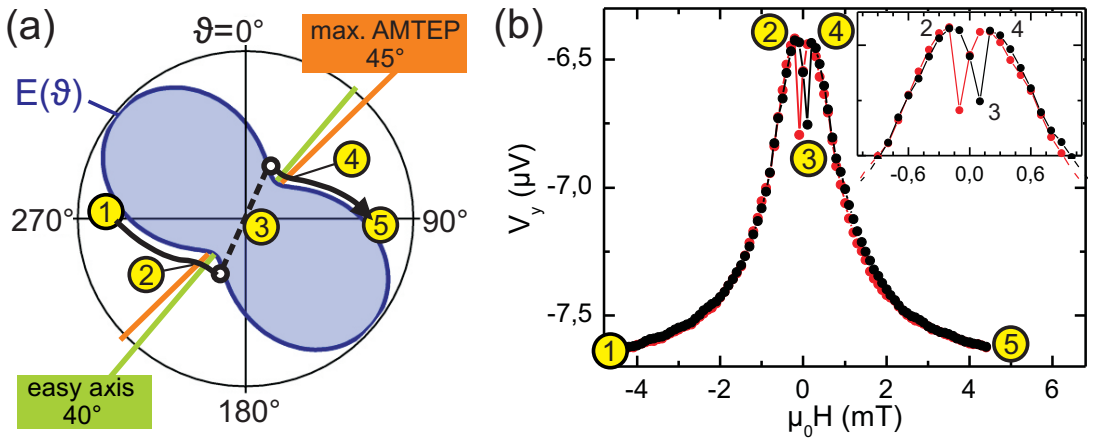

Figure 3.7: (a) Polar plot of the energy landscape with respect to the magnetization angle ϑ. (b) V_y vs. external field for $\theta = 90°$ extracted from Fig. 3.5. (a)&(b) The numbers and the black line display the magnetization reversal process.

in section 4.8. The small deviation of $\Delta(\theta)$ from the $\cos\theta$ fit seen in Fig. 3.6(b) can be related to a small parasitic magnetic field also addressed in section 4.8.

3.4.3 The prominent peak dip structure

In the following, we focus on the middle part of the voltage traces. Since the peak dip structure has a period of 180°, its origin is most likely the AMTEP. In order to understand the complex signatures during the magnetization reversal process, we take a closer look at the measurement for $\theta = 90°$. Here, the Δ contribution is reduced to a minimum and we can concentrate purely on the AMTEP. As shown in Fig. 3.5, the Py layer has a uniaxial anisotropy with an easy axis at an angle of about $\theta_e = 40°$, originating from a small residual magnetic field during the deposition process [54, 55].

The expected magnetic reversal process for this configuration is sketched in Fig. 3.7(a) and is described as follows: Starting near negative saturation, the angle of the magnetization ϑ of the single domain state Py layer with respect to the -x-axis is aligned along the external magnetic field: $\vartheta = \theta = 90° + 180°$. While reducing $\left|\vec{H}\right|$, $\vec{M}$ starts to rotate counterclockwise from $\vartheta = \theta = 90° + 180°$ to the direction of $\theta_e = 220°$, until for $\vec{B} = 0$ the magnetization is aligned along θ_e. When increasing $\vec{H}$ along $\theta = 90°$, $\vec{M}$ starts to rotate away from θ_e until it jumps from about $\vartheta = 210°$ to about $\vartheta = 30°$ via formation of a multi domain state. After the single domain state is recovered, $\vec{M}$ rotates clockwise to its final position at $\vartheta = \theta = 90°$. During the back sweep, $\vec{M}$ turns in an analogous way from $\vartheta = +90°$ to $\vartheta = 90° + 180°$, closing the hysteresis loop with the multi

domain state.

In order to evaluate the corresponding trace $V_y(\theta)$ with respect to the above magnetization reversal process, we take A_0 and c from the fit in Fig. 3.6 as well as the functional dependence

$$V_y = 2A_0 \sin\vartheta \cos\vartheta + c \tag{3.8}$$

Fig. 3.7(a) shows a sketch of the path of ϑ during the upsweep. Fig. 3.7(b) shows the V_y trace for $\theta = 90°$ extracted from the measurement shown in Fig. 3.5. By following the path of ϑ we can construct $V_y(\theta)$ in relation to $\vec{H}$. Starting at point 1 $\vartheta = 270°$, V_y increases until it reaches its maximum (point 2, $\vartheta = 225°$) and then drops down until the switching field is reached (point 3, $\vartheta = 200°$). Here, ϑ turns by 180° via a multi domain state. After the recovery of the single domain state, $\vartheta = 20°$. The rotation of ϑ by 180° is not affecting V_y due to its period of π. Now following the black arrow in Fig. 3.7(a), V_y increases again until it reaches its maximum (point 4, $\vartheta = 45°$) and then relaxes to its starting value (point 5, $\vartheta = \theta = 90°$).
For different angles θ and θ_e the curves will look different but are all well explained by the AMTEP. Meier et al. [56] explain the voltage traces of an identically prepared sample in a similar way and come to the same result. Thus, the peak dip structure is arising naturally from the AMTEP.
Looking at Fig. 3.5, for every angle θ the peaks tend to the same value near the AMTEP maximum. This circumstance is due to the magnetic easy axis being close to 45° where the AMTEP has its maximum. Thus, at zero external field, $\vec{M}$ points along θ_e which is in our case near the AMTEP maximum.

4 Experimental results

4.1 Reversal of the temperature gradient

As described in section 3.4.2, the Δ signal shows a $\cos\theta$ dependence which is consistent with the expected dependence of the TSSE and an amplitude Δ_0 in the range of several tens of nV. Fig. 4.1(a)&(b) show A and Δ vs. θ extracted from the data of Fig. 3.5 with T_1= 343 K and T_2 = 293 K. The average value A shows - as described in detail in section 3.4.2 - a $2A_0 \sin\theta\cos\theta + c$ dependence with an amplitude of 0.8 µV. The difference Δ can be described by $\Delta_0 \cos\theta$ consistent with the expected θ dependence of the TSSE and the ANE. However, the amplitude of $\Delta_0 = (36 \pm 6)$ nV is orders smaller in magnitude than expected from [7]. Note that our measurements are directly comparable to the measurements of Uchida et al. [7]. In order to test if the $\cos\theta$ dependence we observe originates from the TSSE, we reverse the temperature gradient. Fig. 4.1(c)&(d) show $A(\theta)$ and $\Delta(\theta)$ for T_1= 293 K and T_2 = 343 K. As expected, the AMTEP amplitude A_0 changes sign when reversing ΔT:

$$A_0(-\Delta T) \approx -A_0(\Delta T) \tag{4.1}$$

In contrast, Δ only shows a small $\Delta_0 \cos\theta$ dependence with $\Delta_0 = (-6 \pm 6)$ nV compared to the (36 ± 6) nV for T_1= 343 K and T_2 = 293 K.

As seen in Fig. 4.1(d), we observe an oscillation in $\Delta(\theta)$ of higher frequency with an amplitude comparable to the noise level. The green lines in Fig. 4.1 indicate this contribution which, at first sight, can neither be linked to the 2π period of the ANE and TSSE nor to the period of π of the AMTEP. As will be shown later (section 4.8), this contribution can be explained as an asymmetric artifact of the symmetric AMTEP signal, obscuring the Δ signal for higher ΔT. For $\Delta T \leq 50$ K this contribution does not influence the results of the chosen $\Delta_0 \cos\theta$ fit function within the error limit of 10 nV. Due to this reason we stay with the $\Delta_0 \cos\theta$ fit function and refer to section 4.8 for a detailed discussion on the AMTEP artifacts.

Reverting to the results of the reversed temperature gradient, the $\Delta_0 = (36 \pm 6)$ nV for the strip located at the hot side and the $\Delta_0 = (-6 \pm 6)$ nV for the strip located

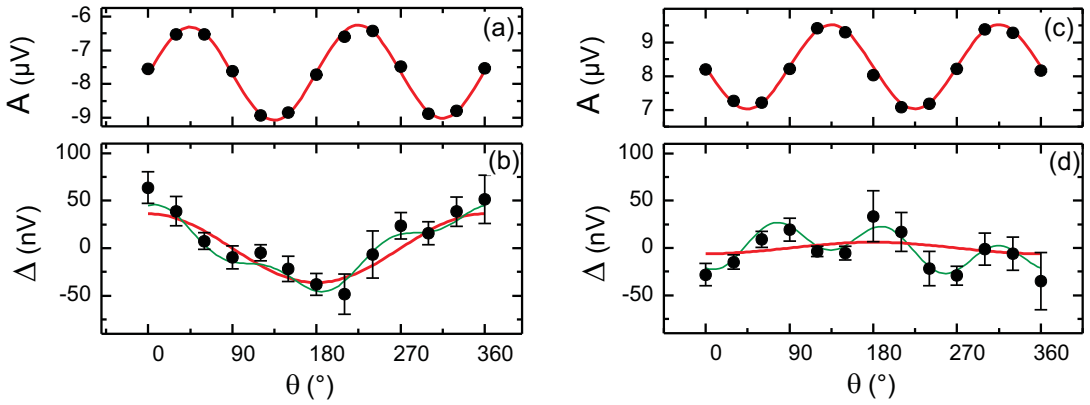

Figure 4.1: A and Δ vs. θ for (a)&(b) T_1= 343 K and T_2 = 293 K and (c)&(d) T_1= 293 K and T_2 = 343 K. The red lines show the $2A_0 \sin\theta\cos\theta + c$ and $\Delta_0 \cos\theta$ fits; Sample type B (Pt/Py/MgO), $x_{\text{strip}} = 1$ mm. The green lines indicate an oscillation in the Δ signal which will be addressed in section 4.8.

at the cold side are not consistent with the sign reversal of Δ_0 expected for the TSSE. Thus, this behavior cannot be explained by the TSSE alone. One possible reason could be that the signal is composed of the TSSE and another constant contribution with the same angular dependence as observed by [40]. This would lead to an asymmetry of the TSSE signal when moving the strip from hot to cold. If this additional contribution is of the same magnitude as the TSSE signal itself, it would reduce or even cancel the signal at one of the sides as observed here. On the other hand, the cosine shape of Δ is observed for the strip located on the hot side and lost at the cold side which is near room temperature (RT). This could be a hint to an interaction of the measurement with the setup leading to a systematical error.

The experimental test is to perform measurements without an in-plane temperature gradient ($(\vec{\nabla}T)_x = 0$) with T_1= T_2 = 293 K and T_1= T_2 = 343 K. The results are shown in Fig. 4.2. Without an in-plane thermal gradient as the driving force, $A_0 \approx 0$ for both cases. This should also be the case for the TSSE. The cosine dependence in Δ ($\Delta_0 = (5 \pm 4)$ nV) for T_1= T_2 = 293 K (Fig. 4.2(d)) is indeed close to 0. However, we see a strong cos dependence at elevated base temperature ($T_1 = T_2 = 343$ K, Fig. 4.2(b)) with $\Delta_0 = (34 \pm 4)$ nV similar to the strip being located at the hot side (T_1= 343 K and T_2 = 293 K, Fig.4.1(b)). This unambiguously demonstrates that the signal cannot originate from the TSSE, as the TSSE should be absent for $(\vec{\nabla}T)_x = 0$ [7, 38]. This leaves the following question: What is the origin of the cosine dependence of the difference signal Δ?

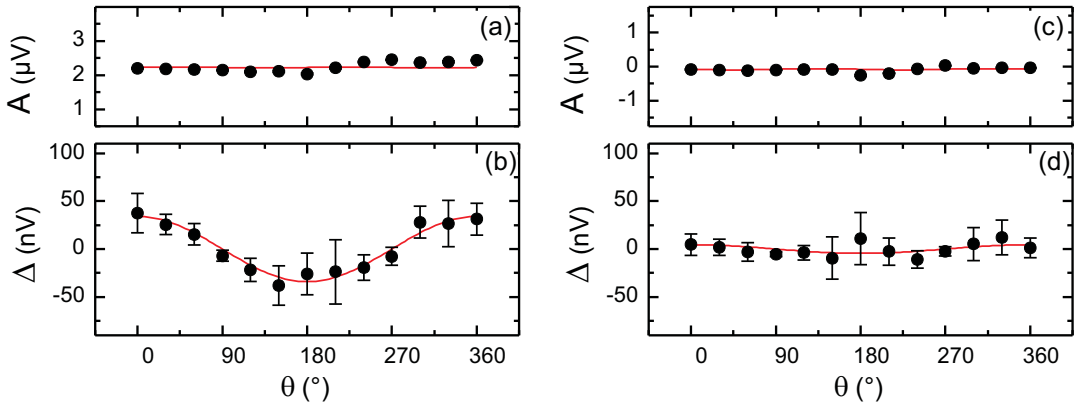

Figure 4.2: A and Δ vs. θ for (a)&(b) T_1= 343 K and T_2 = 343 K and (c)&(d) T_1= 293 K and T_2 = 293 K. The red lines show the $2A_0 \sin\theta\cos\theta + c$ and $\Delta_0 \cos\theta$ fits; Sample type B (Pt/Py/MgO), $x_{\text{strip}} = 1$ mm.

4.2 Spurious anomalous Nernst effect contribution

One possible and most likely candidate for the origin of this cosine dependence is the ANE. As described in section 2.2.2, the origin of an ANE contribution has to be a finite out-of-plane temperature gradient $(\vec{\nabla}T)_z \neq 0$. One reason for this out-of-plane $\vec{\nabla}T$ might be an imbalance of the thermal conductivities as addressed in section 2.4.5. However, in this case one would expect a reversal of $(\vec{\nabla}T)_z$ when reversing $(\vec{\nabla}T)_x$ and thus an inverted ANE signal. This is not observed. Additionally, in the case of $(\vec{\nabla}T)_x = 0$ there is no driving force for $(\vec{\nabla}T)_z$ and thus no ANE. In contrast, we observe a TSSE/ANE like signal at $(\vec{\nabla}T)_x = 0$ at elevated base temperatures. This proves that in our measurements, the possible mismatch of the thermal conductivities is not producing a considerable $(\vec{\nabla}T)_z$ inside the Py layer.
The next option to introduce a perpendicular temperature gradient ($(\vec{\nabla}T)_z \neq 0$) in the sample is the interaction of the sample with the surrounding setup. This option may explain the missing $\cos(\theta)$ contributions to Δ near RT and their observation at higher temperatures. Since we measure in vacuum with the lack of convection cooling, the only possibility to introduce $(\vec{\nabla}T)_z \neq 0$ is the heat transfer via the Au bond wires and the interaction of the sample with the vacuum chamber via surface to surface radiation.

4.3 Varying the base temperature

To verify the idea of a thermal coupling of the sample to the setup, datasets at different base temperatures and different temperature gradients are measured.

T_1(K)	T_2(K)	ΔT(K)	Δ_0(nV)	A_0(µV)
323	273	+50	19±5	0.95±0.05
273	323	-50	-16±4	-0.65±0.05
343	293	+50	36±6	1.40±0.04
293	343	-50	-6±6	-1.25±0.03
373	323	+50	87±12	0.78±0.1
323	373	-50	20±8	-1.01±0.07
403	353	+50	118±9	0.44±0.34
353	403	-50	36±5	-0.72±0.06
283	283	0	-11±3	-0.09±0.06
293	293	0	4±4	-0.02±0.04
343	343	0	34±3	0.01±0.07

Table 4.1: Δ_0 and A_0 for several pairs of T_1 and T_2. $T_1 - T_2$ is either +50 K, −50 K or 0 K.

In detail, a temperature difference of +50 K, 0 K and -50 K is applied between the Cu-pads and measured for different pairs of T_1 and T_2 as listed in table 4.1. The measurements complete the picture of section 4.1. We can observe a TSSE like signal which, in general, does not change sign for reversed $(\vec{\nabla}T)_x$ and has amplitude values in the same order of magnitude even for $(\vec{\nabla}T)_x = 0$. Furthermore, the signal increases for higher T_1, giving further evidence of a coupling to the surrounding. In contrast, A_0 is changing sign for opposite $(\vec{\nabla}T)_x$ and vanishes for $(\vec{\nabla}T)_x = 0$.

To get a better view of the data, we plot Δ_0 and A_0 in respect to T_1, the temperature of the Cu-pad next to the strip in Fig. 4.3(a). However, in the picture of the sample interacting with the setup as described in section 4.2, it is not T_1 that determines the thermal exchange to the surrounding, but the temperature on the sample at the position of the strip T_{strip} which should be the relevant temperature. This means that for T_1 being the cold side T_{strip} is higher than T_1 and for T_1 being the hot side T_{strip} is lower than T_1. Since the strip is located at about 1 mm distance from the edge of the Cu Pad and the gap between both Cu-Pads is $x_{\text{gap}} = 7$mm, T_{strip} can be estimated by the equation

$$T_{\text{strip}} = T_1 + \left[t_{\text{loss}} - \frac{x_{\text{strip}}}{x_{\text{gap}}} \left(1 + 2t_{\text{loss}}\right) \right] (T_1 - T_2) \tag{4.2}$$

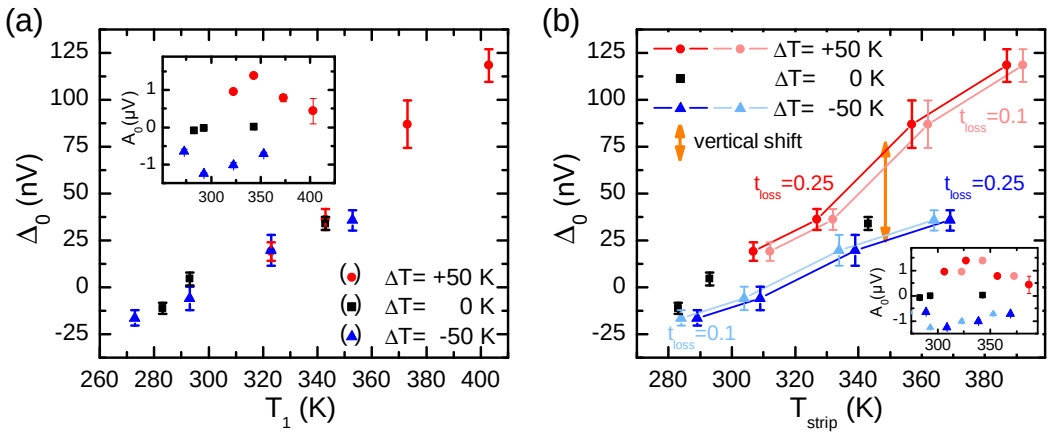

Figure 4.3: (a) Δ_0 vs. T_1 for three different ΔT. The inset shows A_0 vs. T_1. (b) Same data as (a) but the data is referenced to T_{strip} using two different loss coefficients $t_{\text{loss}} = 0.25$ and $t_{\text{loss}} = 0.1$; Sample type: B (Pt/Py/MgO), $x_{\text{strip}} = 1\,\text{mm}$.

where $t_{\text{loss}} = \Delta T_{\text{loss}}/(T_1 - T_2)$ is introduced as a dimensionless factor for the thermal losses at the contacts of the sample to the Cu-Pads. In reference measurements, thermocouples have been attached at the ends of a dummy sample in order to determine the thermal losses at the gluing interfaces and at least 10 percent up to 25 percent ($t_{\text{loss}} = 0.1 - 0.25$) of ΔT is lost at one interface. The losses are symmetrically distributed to both gluing interfaces. With this knowledge, we can reference the data of table 4.1 to a realistic temperature of the strip T_{strip}. The data for $t_{\text{loss}} = 0.25$ and $t_{\text{loss}} = 0.1$ are plotted in fig 4.3b. The data points for $\Delta T = +50\,\text{K}$ (in comparison to fig 4.3a) shift horizontally to the left and the data points for ΔT = -50 K shift to the right. As displayed in fig 4.3b this leads to a vertical gap between the two $(\vec{\nabla}T)_x$ directions. Thus, for one certain T_{strip} there is an up or down shift of the data points for $\pm(\vec{\nabla}T)_x$ with respect to the $(\vec{\nabla}T)_x = 0$ data points. Since there is little difference for the vertical shift between $t_{\text{loss}} = 0.25$ and $t_{\text{loss}} = 0.1$, in the following we relate to $t_{\text{loss}} = 0.25$ as the upper limit of the shift.

In summary, when relating the measured data to T_{strip}, the difference signal Δ_0 shows increasing values for increasing T_{strip}. This dependence seems to be independent of an applied temperature gradient. Additionally, the data points are shifted up or down for opposite $(\vec{\nabla}T)_x$ with respect to the $(\vec{\nabla}T)_x = 0$ data points. This shift may be related to the TSSE as it shows one of its main features, the change of sign when reversing $(\vec{\nabla}T)_x$. Nevertheless, the signal is of the order of a few tens of nV and thus orders smaller than reported for similar measurements by Uchida et al. [7].
Thus, until now there are two questions left open: What is the origin of the monotonous dependence of Δ_0 on T_{strip}? Is the vertical shift feature related to

the TSSE? These two main points are addressed in the following.

4.4 The influence of the electrical contacts

In section 4.2, the coupling of the sample to the surrounding is described as a possible reason for the finite Δ_0 values for $(\vec{\nabla}T)_x = 0$. This coupling may at first glance be mediated by the Au contact wires. In order to check whether the contact wires influence the measurements, we change the sample layout to type C which creates the possibility to contact the Pt strip at the end of the sample (as shown in Fig. 4.4(a)) and thus to neglect any influence of the contact wires to the temperature profile of the sample.

Fig. 4.4(b) shows the results for several pairs of T_1 and T_2. Again, A_0 changes sign for reversed $(\vec{\nabla}T)_x$ and vanishes for $(\vec{\nabla}T)_x = 0$. However, its value of about $0.4\,\mu\mathrm{V}$ is smaller in comparison to the data obtained for samples on the MgO substrate. Since the AMTEP is very sensitive to the layer thickness [57] and since the sample was prepared in a different sputtering chamber, a small difference in the layer thickness of the Py layer due to calibration errors of the deposition rates is a possible reason for this deviation. The difference signal Δ_0 exhibits qualitatively the same dependence on T_{strip} as observed for the sample with a directly contacted Pt detector strip. We observe finite values for $(\vec{\nabla}T)_x = 0$, increasing for greater T_{strip} and a shift of the data points for $\pm(\vec{\nabla}T)_x$. This proves that the contact leads cannot be the origin of a finite $(\vec{\nabla}T)_z$ and yet another mechanism must thermally connect the sample to the surrounding. As mentioned before, surface to surface radiation is a possible reason and is therefore addressed in the next section.

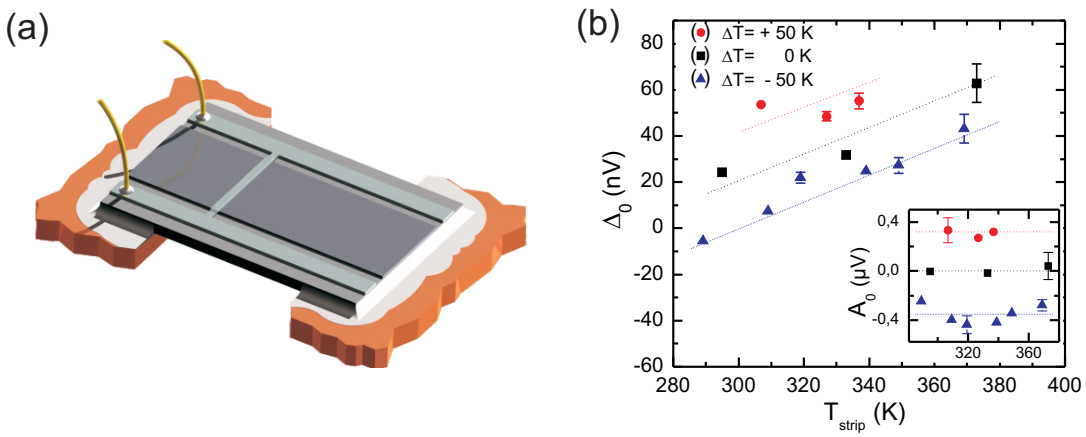

Figure 4.4: (a) Schematic of the sample mounting and electrical contacting of type C samples. (b) Δ_0 vs. T_{strip} for three different ΔT. The inset shows A_0 vs. T_{strip}. Sample type C (Pt/Py/GaAs), $x_{\mathrm{strip}} = 1\,\mathrm{mm}$.

4.5 Thermal radiation model

Since we do not observe a significant change when changing the contact conditions to the detector strip, radiation cooling/heating of the sample producing a finite $(\vec{\nabla}T)_z$ and thus an ANE contribution to Δ is expected. As there is no possibility to directly measure this contribution, a Finite Element Model (FEM), calculated in COMSOL, is used. The major challenge is the extreme aspect ratio of 10^{-6} between the lateral dimension in the mm scale and the layer thicknesses in the nm scale. At first, a 2D model, as sketched in Fig. 4.5(a), is used. The drawback of this model is the long computation time and the limited resolution along the z-direction due to a limited finite element size. Therefore, the thickness of the Py layer cannot be set to 20nm but is limited to a few 100 nm. In order to circumvent these computational limitations, we switched to a 1D model as shown in Fig. 4.5(b). We carefully checked the results for our strip position and found that this model is in good agreement with the 2D model. Only close to the Cu pads at each of the sample sides, where the heat flow has a large z component, the models differ.

After developing the FEM, the calculation for the different T_{strip} used in the measurements is performed and $(\vec{\nabla}T)_z$ inside the Py layer is determined. As shown in Fig. 4.6(a), $(\vec{\nabla}T)_z$ increases monotonically with increasing T_{strip} with values from about -2 to 10 K/m. This means that the radiation cooling effect leads to a temperature difference of the order of 100 nK from top to bottom in the 20 nm thick Py layer. Taking equation 2.22 and the sample dimensions into account, the calculated $(\vec{\nabla}T)_z$ can be connected to the expected Δ_0 values originating from the ANE using

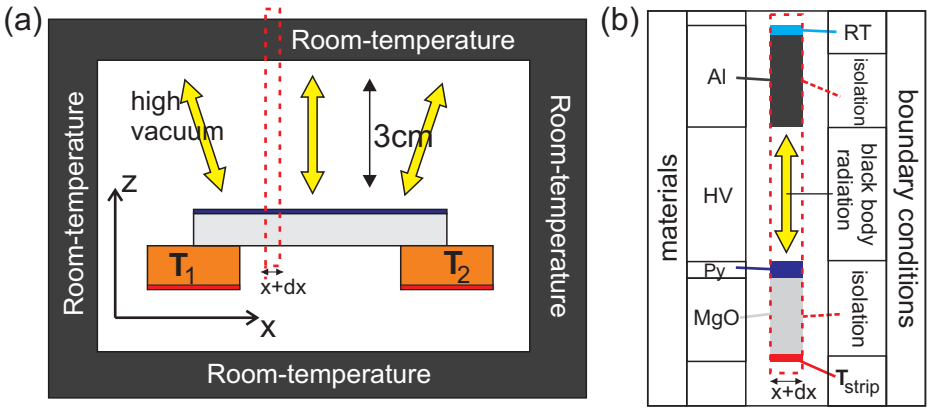

Figure 4.5: (a) Schematic of the 2D FEM model including surface to surface radiation indicated by yellow arrows. (b) Detailed view of the 1D FEM simulation model including materials and boundary conditions.

$$\Delta_0 = \int_0^l E_y dy = \alpha_{\mathrm{ANE}} l (\vec{\nabla} T)_z \tag{4.3}$$

with l being the width of the Py layer, i.e. the length of the detector strip, which in our case is 4 mm. The results are plotted together with the data from Fig. 4.3 for the Pt/Py/MgO sample in Fig. 4.6(b). It turns out that 100 nK per 20 nm are sufficiently high to produce voltages of the order of the measured data. Also, the dependence on T_{strip} fits to our measurements quite well. However, it has to be mentioned that our simple black body model may vary in magnitude by some factor, but despite this point, the FEM model is in good agreement with the measured data and explains the overall slope of the data points, especially the finite values of Δ_0 for increasing T_{strip}. Nevertheless, the model is not able to explain the vertical shift of the data points for opposite $(\vec{\nabla} T)_x$. Thus, this shift may still originate from the TSSE.

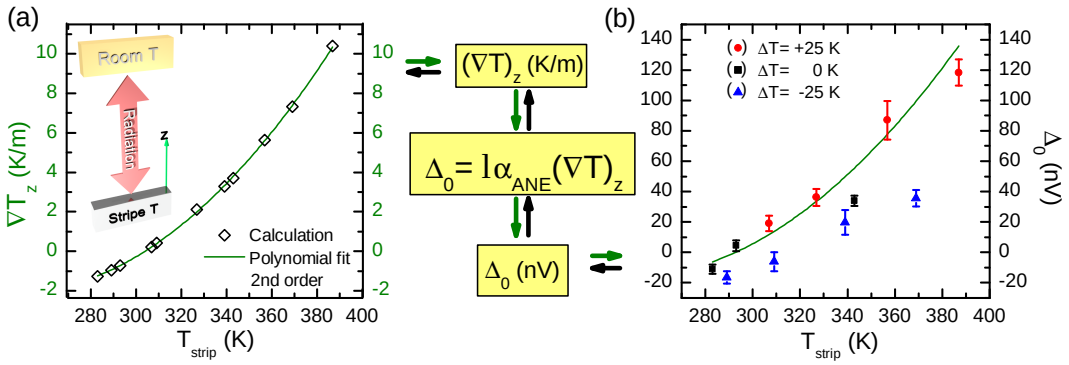

Figure 4.6: (a) Simulated out-of-plane temperature gradient $(\vec{\nabla}T)_z$ vs. T_{strip}. (b) Δ_0 vs. T_{strip} from fig 4.3 including the calculated ANE for $(\vec{\nabla}T)_z$ from (a).

4.6 Control measurements

In this section, the possible contribution of the TSSE to the Δ_0 signal, represented by the vertical shift of the Δ_0 for $\pm(\vec{\nabla}T)_x$, is addressed. We find that the shift occurs for MgO as well as for GaAs substrates and cannot be explained by the FEM model including the ANE and the out-of-plane temperature gradient. To test whether the contribution arises from the ISHE inside the Pt detector strip, two control measurements are performed. One exchanging the Pt strip with a Cu strip (sample type A) and the other one measuring the voltage directly on the Py layer (contacted with Au pads, sample type D). For the first control experiment Cu was chosen as a metal with extremely low spin orbit interaction/long spin diffusion length [58,59] and thus low spin Hall angle and no measurable ISHE. In Fig. 4.7(a) we show the results for the Cu detector strip. A_0 shows the familiar picture and Δ_0 also shows the familiar vertical shift for $\pm(\vec{\nabla}T)_x$. This proves that this reversing signal is not related to the TSSE but has to be of different origin.

In order to check if the detector strip itself influences the measurements, we use two Au contact pads in order to directly contact the Py layer. Fig. 4.7(b) shows the results for these measurements which again exhibit qualitatively the same dependencies for A_0 and Δ_0. At the end of the measurement series on Py a loss of thermal contact is observed. Consequently all affected data points have been deleted. The data points displayed in brackets in Fig. 4.7(b) display the beginning loss of thermal contact and thus are of lower magnitude than expected. Nevertheless, we obtain enough data to observe that the values of A_0 and Δ_0 are a factor of 2 larger in comparison to the measurements with detector strip. This increase can be explained by the missing electrical short circuit of the detector strip itself. Since the measured voltages do not arise from spin orbit effects in the detector strip (as shown in this section), but are generated in the Py layer,

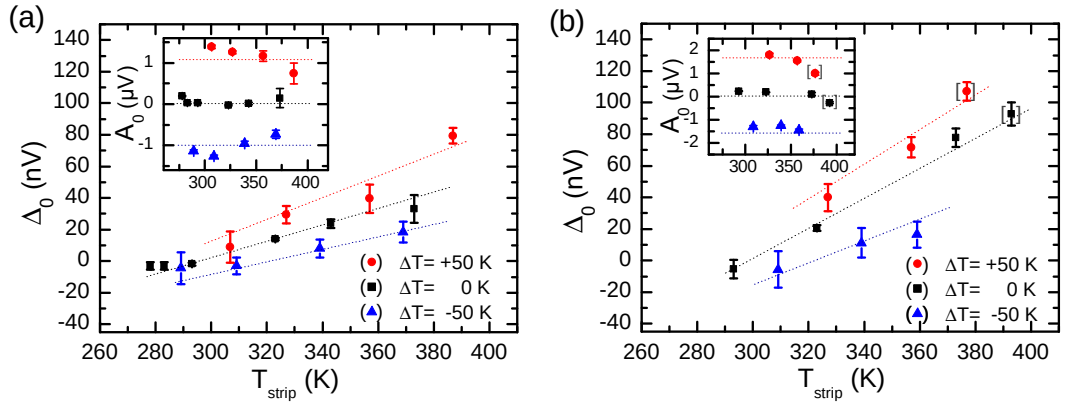

Figure 4.7: Δ_0 vs. T_{strip} for three different ΔT. The insets show A_0 vs. T_{strip}. (a) Sample type A (Cu/Py/MgO), $x_{\text{strip}} = 1\,\text{mm}$. (b) Sample type D (Py/MgO), $x_{\text{strip}} = 1\,\text{mm}$. The data points in brackets display the start of loss of thermal contact.

the attached detector strip allows a back flow of electrons and thus reduces the measured voltages.

4.7 Varying the temperature difference at fixed strip temperature

We have demonstrated that the finite Δ_0 for $\Delta T = 0$ is related to an out-of-plane temperature gradient. After the control experiments without Pt, we know that the additional vertical shift is not related to the TSSE. In order to investigate the origin of this shift, we increase the in-plane temperature gradient $(\vec{\nabla}T)_x$, leaving T_{strip} fixed once for the strip located at the hot side and once for it being located at the cold side. By solving equation 4.2 for T_2, one obtains the temperature pairs T_1 and T_2 fulfilling this condition:

$$T_2 = T_1 - \frac{(T_{\text{strip}} - T_1)}{\left[t_{loss} - \frac{x_{\text{strip}}}{x_{gap}}\,(1 + 2t_{loss})\right]} \tag{4.4}$$

Taking the maximum temperature range of T_1 and T_2 of about 283 K to 413 K and t_{loss} up to 25% into account, we choose for the hot side a T_{strip} of 360 K and for the cold side a T_{strip} of 323 K. The temprature pairs T_1 and T_2 are calculated by assuming $x_{\text{strip}} = 1.5\,mm$ and $x_{gap} = 7\,\text{mm}$. However, the control measurements after opening the chamber reveal a x_{strip} of 0.8 mm. This discrepancy of x_{strip} leads to a shift of T_{strip} for bigger ΔT. Nevertheless, we can express the functional dependence of $T_{\text{strip}}(\Delta T)$:

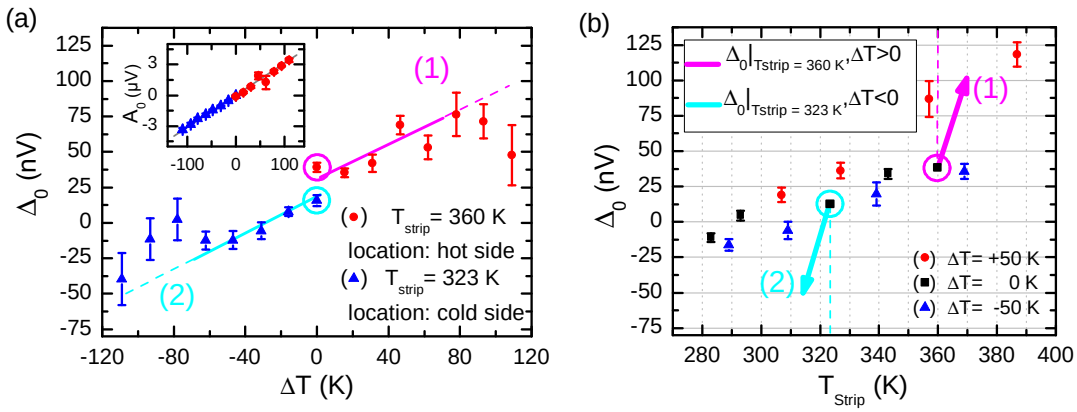

Figure 4.8: (a) Δ_0 vs. ΔT for two different T_{strip}. The inset shows A_0 vs. ΔT. Sample type B (Pt/Py/MgO), $x_{\text{strip}} \approx 1$ mm. The pink and light blue lines are guides to the eye. (b) Copy of Fig. 4.3, Sample type B (Pt/Py/MgO), $x_{\text{strip}} \approx 1$ mm. The pink and light blue arrows display the data of (a)(constant T_{strip}) in the constant ΔT regime of (b).

$$T_{\text{strip}}(\Delta T) = T_{\text{strip}}(\Delta T = 0K) + 0.08\Delta T \tag{4.5}$$

As shown in the following, when taking this dependence into account the systematic error does not change the conclusion of the measurements.

Fig. 4.8(a) presents the measured A_0 and Δ_0 values for the two different T_{strip}. For $\Delta T = 0$ A_0 is expected to be zero and increase/decrease linearly with ΔT for the hot/cold side, independent from T_{strip} in this temperature regime. The inset of Fig. 4.8(a) shows exactly this linear dependence of A_0 values for the two different T_{strip}. Δ_0 shows a linear dependence on ΔT with a big scatter and increasing error above $\Delta T \approx 60$ K. This agrees with the expected increase/decrease with ΔT for the hot/cold side, but Fig. 4.8(a) reveals two different Δ_0 values for $\Delta T = 0$. Taking the measurements from section 4.3, where we varied T_{strip} for fixed ΔT, into account, the different values of Δ_0 for $\Delta T = 0$ originate from the dependence of Δ_0 on T_{strip} due to the ANE. In Fig. 4.8(b) we display the measurements from section 4.3(Fig. 4.3).

In order to be able to compare both measurements one needs to remind that, in this section, we vary ΔT for fixed T_{strip} and in section 4.3 T_{strip} is varied for fixed ΔT. Only in the case of $\Delta T = 0$ the data points (highlighted by circles in Fig. 4.8(a)) can be directly moved from Fig. 4.8(a) to Fig. 4.8(b). The other data points of Fig. 4.8(a) can be indicated in 4.8(b) by the two arrows. These arrows start at $\Delta_0\,|_{\Delta T=0, T_{\text{strip}}=360\,\text{K}}$ and $\Delta_0\,|_{\Delta T=0, T_{\text{strip}}=323\text{K}}$ and display the increasing and

decreasing Δ_0 values for increasing $|\Delta T|$. For constant T_{strip} these arrows point vertically up and down (dashed lines in Fig. 4.8(b)). However, here we need to take into account that due to a systematic error, T_{strip} depends slightly on ΔT. This leads to a tilt of the arrows as shown in Fig. 4.8(a).

So far, the measurements fit well to the data with constant $\Delta T = -50\,\text{K}, 0\,\text{K}, 50\,\text{K}$ and varying T_{strip}. However, by having a closer look to the $\Delta(\theta)$ signal extracted from the raw data, we observe an additional reproducible signal contribution (already indicated in section 4.1) in addition to the $\cos(\theta)$ dependence which is the reason for the big scatter and error in the $\cos\theta$ fit for higher ΔT. As shown in Fig. 4.9, this contribution increases with ΔT. In order to illustrate the deviations of the data points from the $\cos(\theta)$ fit (red lines), we included the green lines which describe the new signal quite well. The fit function of the green line will be explained in detail in the following.

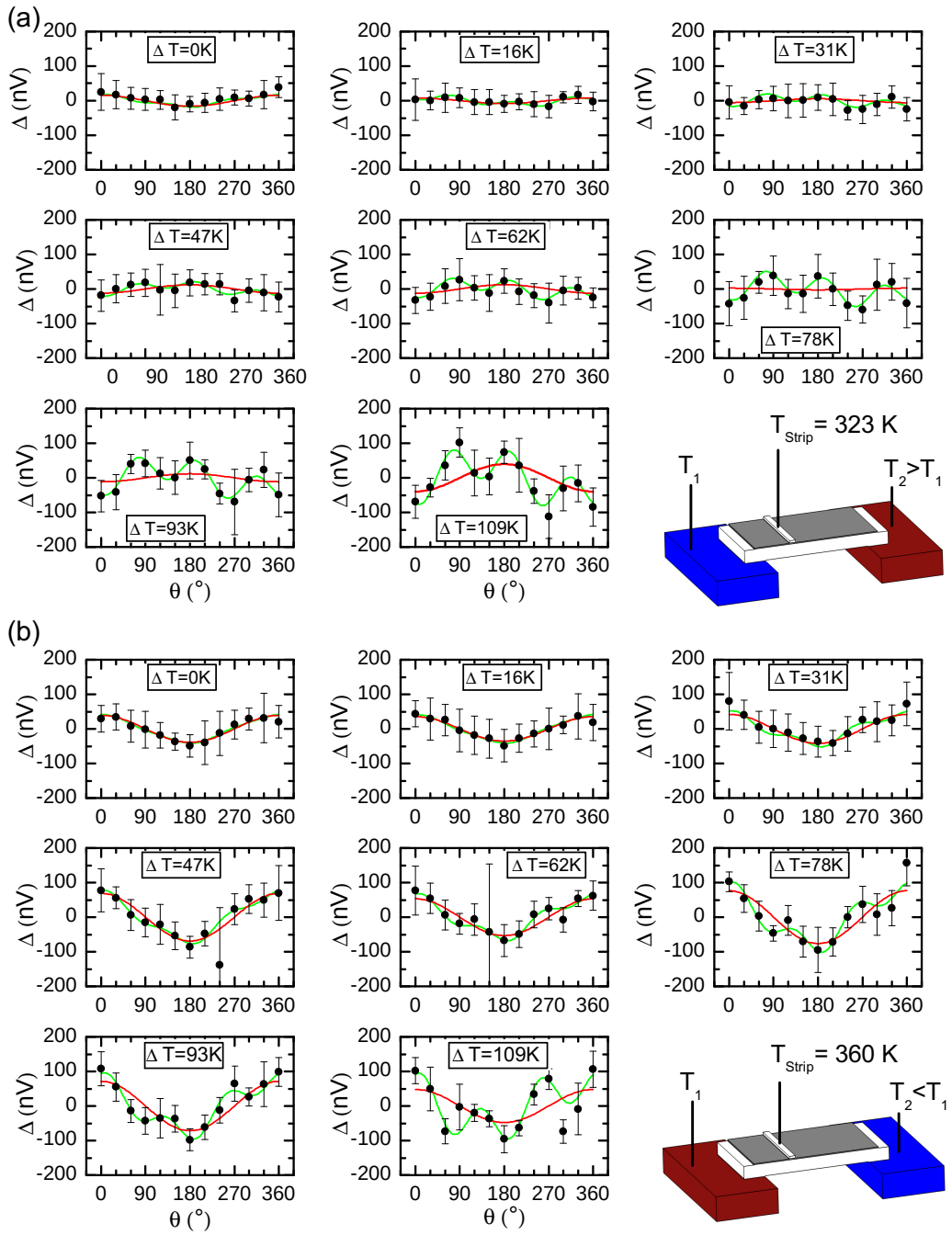

Figure 4.9: (a) Δ vs. θ for decreasing ΔT and $T_{\mathrm{strip}} = 323\,\mathrm{K} + 0.08\Delta T$ (b) Δ vs. θ for increasing ΔT and $T_{\mathrm{strip}} = 360\,\mathrm{K} + 0.08\Delta T$. The red lines show the $\Delta_0 \cos\theta$ fits, the green lines indicate the new arising signal component fitted with the function from section 4.9; Sample type B (Pt/Py/MgO), $x_{\mathrm{strip}} \approx 1\,\mathrm{mm}$.

4.8 The role of a parasitic in-plane magnetic field

As described above, the Δ signal cannot be fitted by a pure $\cos(\theta)$ dependence for higher in-plane temperature gradients $(\vec{\nabla}T)_x$. Since the strip temperature is kept constant and the additional signal scales with ΔT, we might measure an artifact related to the AMTEP. As a possible origin we have a closer look on the influence of parasitic magnetic fields. Test measurements with permanent magnets reveal that a static in-plane magnetic field can produce similar signal contributions. An out-of-plane static magnetic field does not seem to change the signal. The test measurements can only provide a rough picture since there is no exact information on the orientation and magnitude of the parasitic magnetic field. Nevertheless, it leads to the idea of calculating the magnetization orientation including a unidirectional in-plane magnetic field. The energy balance in this case is as follows:

$$\frac{E}{V} = -\vec{M} \cdot \vec{H}_{\text{sweep}} - \vec{M} \cdot \vec{H}_{\text{parasitic}} + K_{\text{u}} \sin^2(\vartheta - \alpha_{\text{easy}}) \tag{4.6}$$

with the Zeeman energy term for the external sweeping field $\vec{H}_{\text{sweep}}$ the parasitic magnetic field $\vec{H}_{\text{sweep}}$ and K_{u} as the uniaxial anisotropy constant. α_{easy} is extracted from the measurement and $K_{\text{u}} = 4.5 \cdot 10^3 \frac{\text{J}}{\text{cm}^3}$ can be extracted from the comparison of calculation and experiment. In the calculation, we combine the first two terms of equation 4.6 and use the effective magnetic field $\vec{H}_{\text{eff}} = \vec{H}_{\text{sweep}} + \vec{H}_{\text{parasitic}}$ and obtain

$$\frac{E}{V} = -M_S H_{\text{eff}} \cos(\vartheta - \alpha_{\text{eff}}) + K_{\text{u}} \sin^2(\vartheta - \alpha_{\text{easy}}) \tag{4.7}$$

with α_{eff} being the direction of $\vec{H}_{\text{eff}}$. In order to calculate the equilibrium position of $\vec{M}$, we first calculate H_{eff} as well as α_{eff} and minimize equation 4.7 numerically. These numerical calculations have been performed along the measured sweep directions θ and sweep values H_{sweep}. The resulting ϑ values are inserted into equation 3.8, which is repeated here as a reminder:

$$V_y = 2A_0 \sin\vartheta \cos\vartheta + c \tag{4.8}$$

using A_0 and c from the measurements to link the calculations with the measured data. Fig. 4.10 shows a comparison between measured data and calculation. It has to be mentioned that the calculated data, in contrast to the measured data, do not include the ANE. In the next step, $\Delta(\theta)$ and $A(\theta)$ are determined from the calculated data. By adjusting the direction and magnitude of $\vec{H}_{\text{parasitic}}$ we

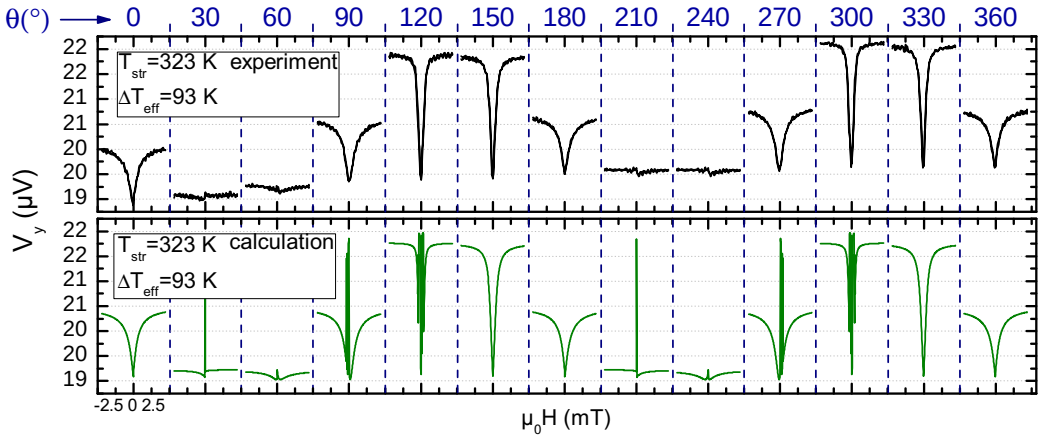

Figure 4.10: The upper panel shows the data from Fig. 3.5; Sample type B (Pt/Py/MgO), $x_{\text{strip}} = 1$ mm. Lower panel: Calculated transverse voltage V_y vs. magnetic field and angle θ, $-4.5\,\text{mT} \leq \mu_0 H \leq 4.5\,\text{mT}$ scaled to the data of Fig. 3.5.

can reproduce the data extremely well. An example is shown in Fig. 4.11(a). It turns out that for our setup we obtain $H_{\text{parasitic}} = 0.03\,\text{mT}$ at an angle of $\alpha_{\text{parasitic}} = 309°$ with respect to the -x-axis. This demonstrates that in-plane fields far below 0.1 mT can produce an asymmetry in the AMTEP signal which is, in our case, contributing to the Δ signal up to tens of nV. For comparison the in-plane component of the earth magnetic field is estimated to $H_{\text{earth}} = 0.02\,\text{mT}$ at an angle of about 90°. Since we used numerical calculations, we cannot obtain a fit function from the calculations. But, as shown in Fig. 4.11(b),

$$\Delta(\theta) = D\cos(\theta) + F\sin(\theta + \delta_1)\cos(2\theta + \delta_2) \tag{4.9}$$

can be taken as a fit function with $\delta_1 = 3.76°$ and $\delta_2 = 46.35°$ and the fit parameters D and F. The green lines in Fig. 4.9 illustrate this fit function applied to the measured data and prove the match to the experiment (including the ANE contribution as shown in section 4.9). Since very small magnetic fields are the origin of these artifacts, we carefully checked the magnetic fields arising from the Peltier elements and found a maximum in-plane field of 0.003 mT. Further taking into account that the calculation with a fixed parasitic field describes the experiment over a broad range of temperatures on the Cu pads and that this broad range of temperatures results in different currents in the Peltier elements and thus different magnetic fields at the sample position, the magnetic field of the Peltier elements can be seen as a minor contribution.

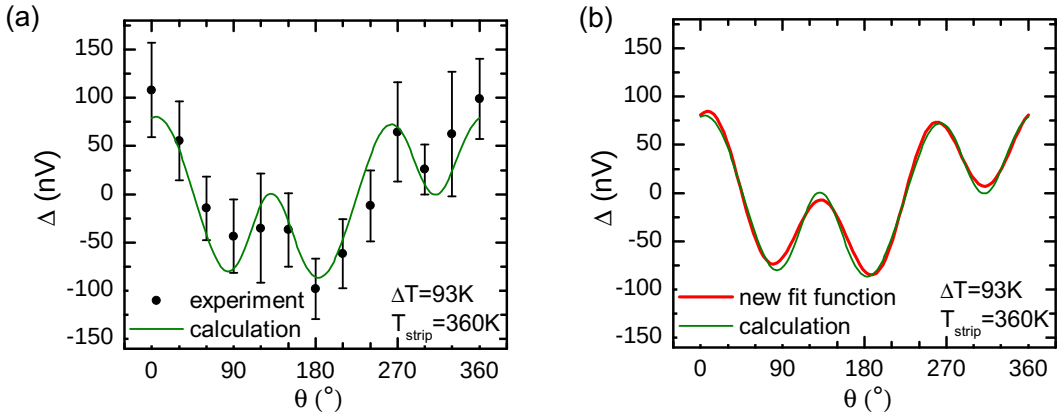

Figure 4.11: (a) Comparison between calculation and measurement for ΔT=93 K and T_{strip}=360 K (b) Fit of equation 4.9 to the calculated data.

4.9 Asymmetric artifacts of the anisotropic magneto-thermoelectric power

In the last section we introduced a small static in-plane magnetic field which explains the arising Δ signal contribution for higher $(\vec{\nabla}T)_x$. We found the fit function

$$\Delta(\theta) = D\cos(\theta) + F\sin(\theta+\delta_1)\cos(2\theta+\delta_2) \tag{4.10}$$

to analyze the new data. However, as mentioned before, the calculation does not include any ANE which is present in the experiment. This means that the correct description of $\Delta(\theta)$ including the ANE is as follows:

$$\Delta(\theta) = \Delta_{0,\text{ANE}}\cos(\theta) + \Delta_{0,\text{AMTEP}}\cos(\theta) + F\sin(\theta+\delta_1)\cos(2\theta+\delta_2) \tag{4.11}$$

with $\Delta_{0,\text{ANE}}$ as the ANE contribution and $\Delta_{0,\text{AMTEP}}$ as the AMTEP artifact. As shown before, $\Delta_{0,\text{ANE}}$ is related to T_{strip} and originates from an out-of-plane temperature gradient. $\Delta_{0,\text{AMTEP}}$, in contrast, does not depend on T_{strip} but scales linearly with A_0. This insight helps us to explain the vertical shift observed in the Δ_0 data points for positive and negative $(\vec{\nabla}T)_x$ in comparison to the Δ_0 data points for $(\vec{\nabla}T)_x = 0$ at different base temperatures as shown in Fig. 4.3, 4.4 and 4.7. There, we used for the evaluation of Δ_0 a simple $\cos\theta$ fit:

$$\Delta(\theta) = \Delta_0\cos\theta \tag{4.12}$$

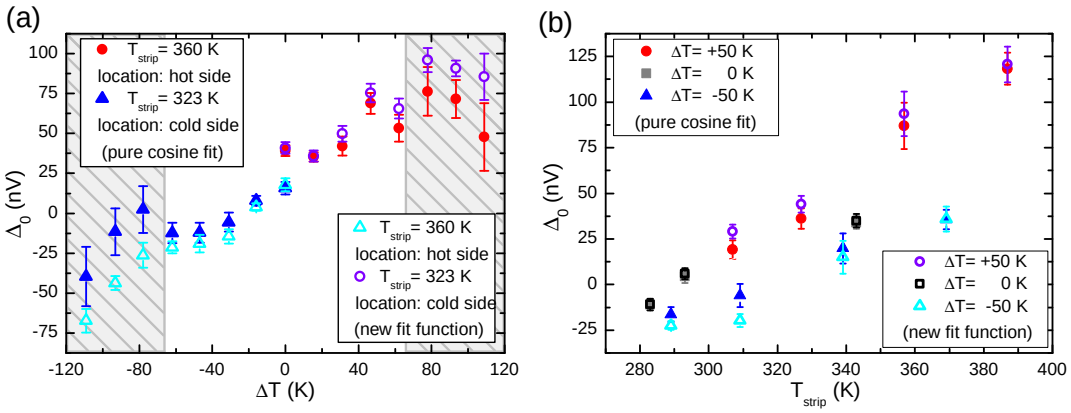

Figure 4.12: (a) Δ_0 obtained from the data of section 4.7 (Fig. 4.8) using the new fit function in comparison to the pure cosine fit. The shaded areas indicate the region of higher deviation of the two fit results. (b) Δ_0 obtained from the data of section 4.3 (Fig. 4.3) using the new fit function in comparison to the pure cosine fit.

By comparison of equation 4.11 with equation 4.12 it becomes obvious that the cos fit cannot distinguish between the ANE and the AMTEP contributions.

$$\Delta_0(T_{\mathrm{strip}}, (\vec{\nabla}T)_x) = \overbrace{\Delta_{0,\mathrm{ANE}}(T_{\mathrm{strip}})}^{\propto T^2_{\mathrm{strip}}} + \overbrace{\Delta_{0,\mathrm{AMTEP}}((\vec{\nabla}T)_x)}^{\propto (\vec{\nabla}T)_x} \tag{4.13}$$

Fig. 4.12(a) displays Δ_0 with respect to ΔT for 2 different T_{strip} (data from section 4.7), using once the $\cos\theta$ fit function and once the new fit function. The gray areas display the regions where the deviation of the two fit functions is bigger than our noise level, which is the case for $\Delta T > 60\,\mathrm{K}$. In general, the new fit function even slightly enhances Δ_0. We also carefully checked the data fitted so far with the $\cos\theta$ fit and found that for temperature differences of $\pm$ 50 K the new fit function changes the results of Δ_0 at maximum by 10 nV, which is within our noise limit. As an example Fig. 4.12(b) shows $\Delta_0(T_{\mathrm{strip}})$ for the data from section 4.3 (sample type B, Pt/Py/MgO) for both fit functions. All this justifies to stay with the cos fit used so far for $\Delta T < 60\,\mathrm{K}$.

On the basis of equation 4.13 and the COMSOL simulations including $(\vec{\nabla}T)_z$, we reconstruct Δ_0 for $\mathrm{sign}(\Delta T) = \{-, 0, +\}$ and varying T_{strip}. The original measurements are shown in Fig. 4.3, 4.4 and 4.7. We start with the variation of T_{strip} and $(\vec{\nabla}T)_x = 0$, thus only the first term of equation 4.13 contributes to Δ_0. The result then is described by the COMSOL simulations from section 4.5 and is plotted in Fig. 4.13(a). Now we switch on the in-plane gradient with the strip at the cold side of the sample ($\mathrm{sign}(\Delta T) = \{-\}$). This adds the second term to Δ_0 and leads to a constant downshift which is indicated by the blue arrows in

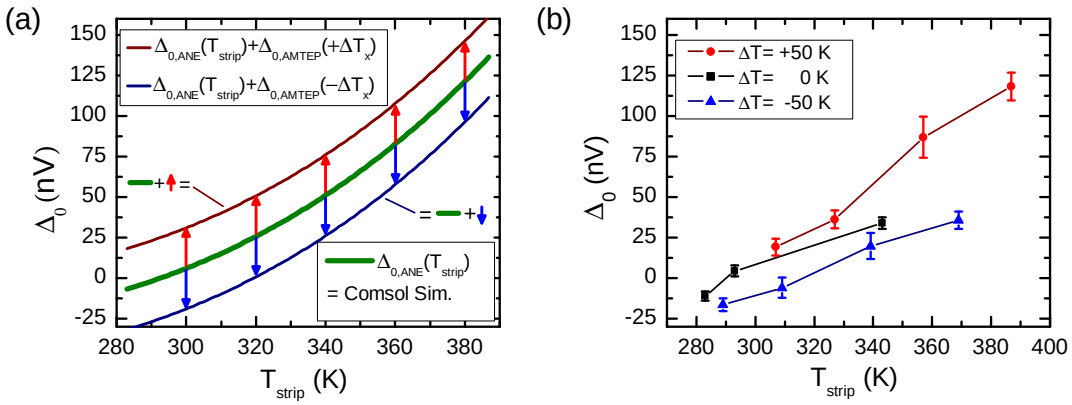

Figure 4.13: Comparison of the expected $\Delta_0(T)$ dependence (a) - including a finite out-of-plane temperature gradient and AMTEP artifacts - and experimental data from section 4.3 (b).

fig 4.13(a). Vice versa, for the strip at the hot side, we get the opposite effect indicated by the red arrows in fig 4.13(a). The magnitude of the up/down shift is extracted from Fig. 4.8. Fig. 4.13(b) shows, as an example, the measured data from section 4.3 on the same scale for comparison. It turns out that our model, including the ANE and the AMTEP artifacts, describes the finite Δ_0 values for $\Delta T = 0$ as well as the vertical shift of the data points for $\pm\Delta T$.

At this point it has to be mentioned that the unexpected asymmetric AMTEP artifacts in the Δ signal get asymptotically smaller for higher sweeping fields $\vec{B}$. Here, the magnetization of the ferromagnetic layer aligns more and more to the external magnetic field thus the contribution of the asymmetric magnetization reversal process to our data processing procedure gets smaller for higher $\vec{B}$ fields. We calculate that the asymmetric AMTEP contribution would be reduced by a factor of four for sweeping fields up to 20 mT and a factor of ten for 50 mT. However, in our setup we are limited to a maximum of 5 mT and cannot check this assumption.

4.10 From bulk substrates to SiN$_x$-membranes

In parallel to the measurements of the TSSE on bulk substrates, we investigate suspended Py films on SiN$_x$ membranes. The sample layout is described in detail in section 3.3.2. Fig. 4.14 presents the transverse voltages V_y recorded at the hot end with a temperature difference of 48 K, applied over the distance of 200 µm with the heat sink of setup 2 set to room temperature. In contrast to the measurements in setup 1 we observe a higher offset value of several 100 µm which is related to the different wire materials with very different Seebeck coefficients as

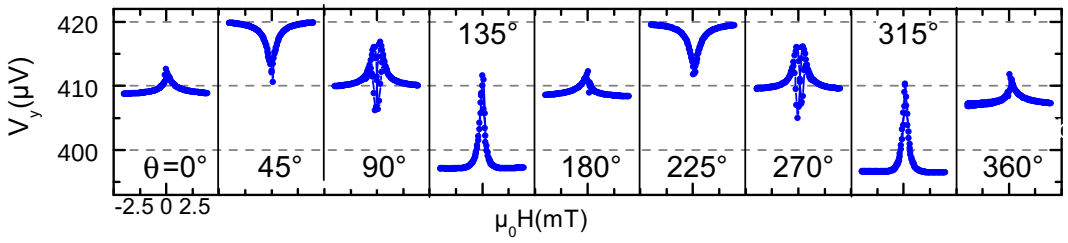

Figure 4.14: Transverse voltage V_y vs. magnetic field and angle θ. $-4\,\mathrm{mT} \leq \mu_0 H \leq 4\,\mathrm{mT}$, T_1=341 K and T_2=293 K. The noise level in each sweep is 50 nV. Sample type: Membrane (Pt/Py/SiN_x) strip at the hot side. Data obtained by Sasmita Srichandan.

there are Aluminum (bond wires), Au plated Cu pads (chip carrier), Constantan (used in the cryostate), and Cu leads. In order to extract the AMTEP value and the difference amplitude Δ_0, we process the data in the same way as the bulk sample measurements. Before showing the results, a short comment to the different shape of the peak dip structure in comparison to the data shown in section 3.4.2 has to be made. The suspended films show an easy axis along $\theta \approx 0°$ so that the signal always tends to $A_0(90°) + c$ which is exactly the offset value of c. The exact shape of the single voltage traces can also be analyzed and explained similar to section 3.4.3 and is not shown here.

Fig. 4.15(a)&(b) show the extracted $A(\theta)$ and $\Delta(\theta)$ from Fig. 4.14. $A(\theta)$ exhibits a pure AMTEP contribution with $A_0 = 11.4\,\mu\mathrm{V}$. Although the Pt strip length of 500 µm is shorter, the large A_0 signal, compared to the bulk samples, is attributed to the 80 times larger $(\vec{\nabla}T)_x$ on the membrane. Fig. 4.14 shows a pure cos fit of the Δ signal and additionally the new fit function from equation 4.11. This asymmetric contribution can already be seen by a closer look on fig 4.14 since for some angles the asymmetry already becomes obvious in the raw data. The fit results in a save upper limit of the pure cos contribution - i.e. the TSSE like signal - of 50 nV.

In the next step, we checked our results by removing the Pt strip and measuring directly the Py film (this time the cold side). Fig. 4.15(c)&(d) show the resulting $A(\theta)$ and $\Delta(\theta)$. $A(\theta)$ shows again a pure $A_0 \sin(\theta)\cos(\theta) + c$ relation, but the amplitude A_0 is about 4 times larger compared to the measurements with the Pt strip. This enhancement is due to the missing short circuit of the Pt strip which seems to be more crucial on the suspended samples than on the macroscopic bulk substrates. A_0 does not change sign since in setup 2, in order to move from the hot to the cold side, the strip has to be replaced in contrast of reversing the temperature gradient in setup 1. The Δ signal is again fitted with a pure cos function and the new fit function from equation 4.11. One can see a change of the signal shape and height in comparison to the Δ signal with Pt strip. The

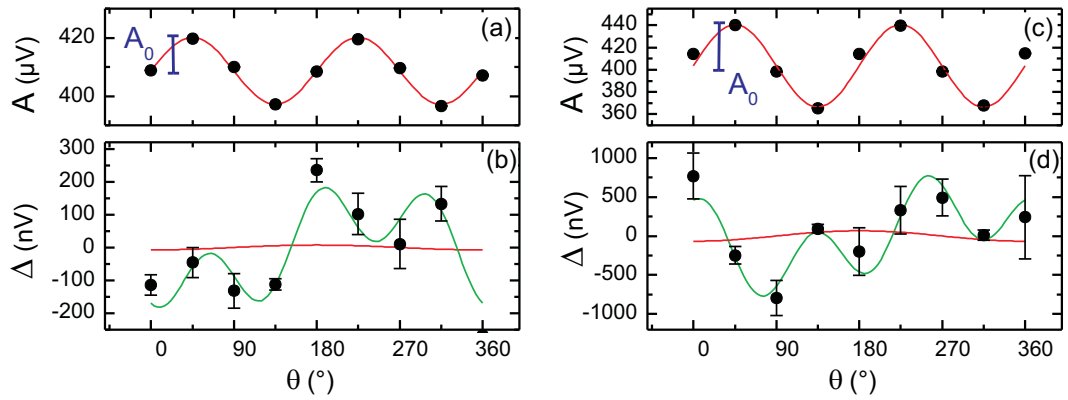

Figure 4.15: A and Δ vs. θ, (a&b) Sample type: Membrane (Pt/Py/SiN_x) strip at the hot side, (c&d) Sample type: Membrane without detector strip (Py/SiN_x), detection points near the cold side. Data obtained by Sasmita Srichandan.

bigger magnitude is related to the lack of the Pt strip. The different shape is described by different phases δ_1 and δ_2 (see section 4.9), indicating a change of the parasitic field between the two measurements. This change may be due to some other setups in the laboratory influencing the measurements with small parasitic magnetic fields. But since the orientation of setup 2 in the laboratory has changed, we are not able to measure the parasitic field at the point of time of the measured data.

5 Discussion

5.1 Lack of the transverse spin Seebeck effect compared to other groups

Concluding our measurements done so far, we can neglect a contribution of the TSSE within the uncertainty of our measurements. The transverse voltage V_y is dominated by the AMTEP and a smaller ANE contribution, both arising from the Py layer. We see no qualitative change in the signal for different substrates and strip materials or even without any detector strip, thus we do not observe an ISHE contribution and thus no TSSE. The TSSE like signals with a $\cos\theta$ dependence are well explained by the ANE and an unexpected asymmetrical artifact of the AMTEP. Comparing the different data sets, we evaluate our uncertainty of a possible TSSE contribution to a safe upper limit of 10 nV for setup 1 and 50 nV for setup 2.

Since in setup 1 we use the same sample dimensions as Uchida et al. [7] the magnitude of the observed signals is easy to compare and we find the upper limit of the TSSE 250 times smaller in comparison to [7]. For measurements with different sample dimensions and especially for the measurements on membranes in setup 2, the resulting voltages need to be scaled to be comparable. For this reason, the spin Seebeck coefficient S_S is introduced as a material parameter which allows us to compare the results [7,40]. Unfortunately, there is no consensus of the exact definition of S_S, so that we will use both common definitions: The more empirical definition by Jaworski et al. [40] (definition 1):

$$S_S = \frac{\Delta V_y \, L}{2 L_{\mathrm{Pt}} \, \Delta T} \tag{5.1}$$

with the transverse voltage change $\Delta V_y = V_y(+) - V_y(-)$ which is equal to $-2\Delta_0$ in our case, the length of the Pt strip L_{Pt} and the distance between the two heat reservoirs L. And the more microscopic definition of Uchida et. al [7] (definition 2):

$$S_S = \frac{\Delta V_y \, d_{\mathrm{Pt}}}{\theta_{\mathrm{SH}} \, \eta_{\mathrm{Py-Pt}} \, L_{\mathrm{Pt}} \, \Delta T} \tag{5.2}$$

	Uchida et al. [7]	Uchida et al. [38]	Avery et al. [60]
ΔV_y	$\sim$10 µV	$\sim$10 µV	<5 nV
ΔT on sample	21 K	21 K	50 K
Definition of S_S	Def. 2 (equ. 5.2)	Def. 2 (equ. 5.2)	Def. 2 (equ. 5.2)
$\theta_{\mathrm{SH}}, \eta$	0.0037, 0.2	0.08, 0.27	0.08, 0.16
Dimensions	L: 6 mm,	L: 6 mm,	L: 900 µm,
	L_{Pt}: 4 mm	L_{Pt}: 4 mm	L_{Pt}: 35 µm
	d_{Pt}: 10 nm	d_{Pt}: 10 nm	d_{Pt}: 10 nm
S_S	$-2 \cdot 10^{-9}\ \frac{\mathrm{V}}{\mathrm{K}}$	$-6 \cdot 10^{-11}\ \frac{\mathrm{V}}{\mathrm{K}}$	$-2.2 \cdot 10^{-12}\ \frac{\mathrm{V}}{\mathrm{K}}^{(*)}$

Table 5.1: Overview of the spin Seebeck coefficients (S_S) published for Py so far. The table includes the main parameters used for the calculation of S_S in each publication. $(*)$ calculated from values Avery et al. used in their comparison [60]

with the spin Hall angle θ_{SH}, the spin injection efficiency $\eta_{\mathrm{Py-Pt}}$ and the thickness of the Pt strip d_{Pt}. Since there is no clear value for θ_{SH}, as described in section 2.1.4, this definition may lead to incomparable results. In table 5.1 we provide an overview of the measured voltage signals, the used definitions and quantities as well as the resulting S_S from [7], [38] and [60]. It is obvious that the different values of θ_{SH} are the reason for the strong deviation of S_S between [7] and [38] in otherwise similar data sets.

In order to compare our measurements to the ones listed in table 5.1 we calculate the spin Seebeck coefficient using both definitions. Furthermore, we take θ_{SH} and $\eta_{\mathrm{Py-Pt}}$ from [7] and [38], as well as the measurement parameters of [7], [38] and [60] and calculate the resulting S_S, as shown in table 5.2. Table 5.2 shows a broad spectrum of S_S within the same data sets depending on which definition and θ_{SH}, $\eta_{\mathrm{Py-Pt}}$ values are used for the calculation. Especially, as definition 1 uses the temperature gradient while definition 2 uses the temperature difference the values differ for small sample sizes as present in samples on SiN_x membranes [60]. Nevertheless, our S_S are orders smaller in comparison to Uchida et al. [7,38] and comparable to Avery et al. [60]. Avery et al. state that „within the 5 nV estimated error of [their] experiment there is no evidence of a signal from the spin Seebeck effect“ [60]. We confirm this statement and also have no evidence for the TSSE in our measurements with bulk substrates as well as in suspended Py films within the uncertainty of our measurements which is 10 nV for setup 1 and 50 nV for setup 2.

S_S	Definition 2 $\theta_{\mathrm{SH}} = 0.0037, \eta = 0.2$	Definition 2, $\theta_{\mathrm{SH}} = 0.08, \eta = 0.27$	Definition 1 [40]
$\Delta V_y, L, L_{\mathrm{Pt}}, \Delta T$ from [7], [38]	$-1.6 \cdot 10^{-9}\ \frac{\mathrm{V}}{\mathrm{K}}$	$-5.5 \cdot 10^{-11}\ \frac{\mathrm{V}}{\mathrm{K}}$	$-3.6 \cdot 10^{-7}\ \frac{\mathrm{V}}{\mathrm{K}}$
$\Delta V_y, L, L_{\mathrm{Pt}}, \Delta T$ taken from [60]	$-3.9 \cdot 10^{-11}\ \frac{\mathrm{V}}{\mathrm{K}}$	$-1.3 \cdot 10^{-12}\ \frac{\mathrm{V}}{\mathrm{K}}$	$-1.3 \cdot 10^{-9}\ \frac{\mathrm{V}}{\mathrm{K}}$
$\Delta V_y, L, L_{\mathrm{Pt}}, \Delta T$ from this work	Bulk: $-1.4 \cdot 10^{-12}\ \frac{\mathrm{V}}{\mathrm{K}}$	$-4.6 \cdot 10^{-14}\ \frac{\mathrm{V}}{\mathrm{K}}$	$-3 \cdot 10^{-10}\ \frac{\mathrm{V}}{\mathrm{K}}$
	Memb.: $-2.8 \cdot 10^{-11}\ \frac{\mathrm{V}}{\mathrm{K}}$	$-9.6 \cdot 10^{-13}\ \frac{\mathrm{V}}{\mathrm{K}}$	$-2.1 \cdot 10^{-10}\ \frac{\mathrm{V}}{\mathrm{K}}$

Table 5.2: Table of Spin Seebeck coefficients S_S taking into account experimental data, the two different definitions and different values of $\theta_{\mathrm{SH}}, \eta$, used in the literature.

5.2 The Pt/Py interface

Since we see no TSSE in our measurements, we have to check every possibility for a suppression of the TSSE in our samples. If the spin current, generated in the Py layer, cannot enter the attached Pt strip, the ISHE and thus the TSSE is not measurable. In order to check the transparency of the interface, one can perform spin pumping experiments, where a line width broadening in the ferromagnetic resonance of the Py is observed, when a spin sink (here Pt) is attached to it [61–63]. If a spin current flows from the Py into the Pt there will be a net loss of angular momentum in the Py layer. This then corresponds to an enhanced damping in the Py and thus a line width broadening in the ferromagnetic resonance measurements (FMR). We perform spin pumping measurements on identical bi-layers produced in the same sputtering chamber as the GaAs substrate samples and the suspended Py layers on SiN_x membranes [27]. We use two types of samples, a Py/Pt bilayer and a Py reference layer, both on GaAs substrates. Both samples are investigated using FMR. We sweep the external magnetic field H_0 for a fixed exciting microwave frequency f and record the absorption of the microwave amplitude. The width of these resonance curves is plotted in Fig. 5.1. From these measurements we evaluate a spin mixing conductance of $3.0 \times 10^{19}\,\mathrm{m}^{-2}$ which is in good agreement with the literature [64]. For more detail we refer to Obstbaum et al. [27]. Coming back to the TSSE measurements we proved the high quatlity of the Pt/Py interfaces produced in our sputtering system and we expect no significant change for the samples produced in Bielefeld under similar conditions, which means fully in situ preparation of the bi-layers.

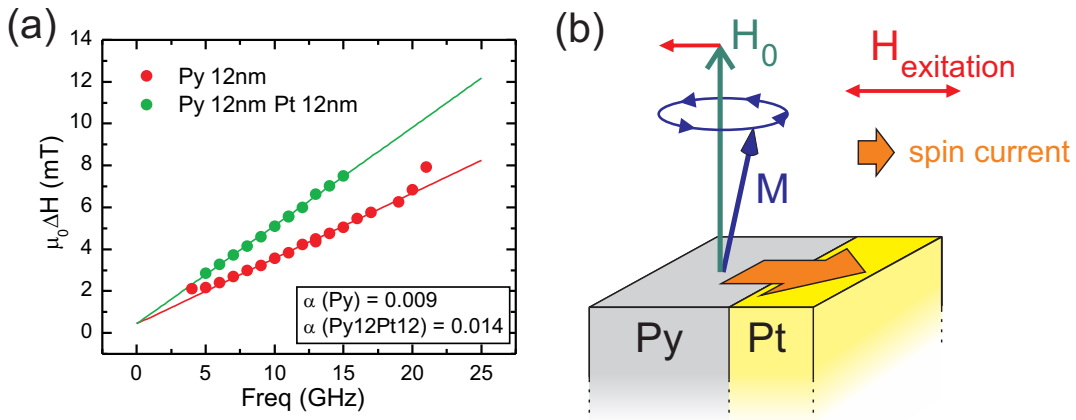

Figure 5.1: (a) Linewidth $\mu_0 \Delta H$ vs. excitation frequency for pure Py films and Pt/Py bi-layers. (b) Sketch of the spin pumping measurement.

5.3 Differences in setups

One main difference from our setup compared to the one used in [7] is the electrical contact to the Pt strip. In our measurements we use thin gold wires to minimize a heat transfer from the electrical contacts to the sample. By using different sample layouts we ensure that the influence is negligibly small (see section 4.4). By contrast, the electrical contacts in the setup of the Saitoh group are produced by Tungsten needles pressed onto the ends of the Pt detector strip. In order to check whether this difference is crucial, we performed test measurements at the University of Bielefeld using contact needles. It turns out that there is a non-reproducible TSSE like contribution observable which seems to be connected to the overall temperature of the setup. Daniel Meier et al. then performed systematic measurements with a heater attached to one of the measuring needles. It turns out that, for a certain heating power, a TSSE like signal can be produced which is, in reality, an ANE contribution originating from an out-of-plane temperature gradient introduced by the contact needles. For a detailed view on the experiment please have a look at Daniel Meier et al. [56]. Additionally the Bielefeld group had the possibility to perform TSSE measurements on their samples in the setup of the Saitoh group in Japan. They reported that they could measure TSSE in some samples in the region of several 100 nV including the exact same sample from section 4.3 in which we observe no TSSE in our setup and neither does the Bielefeld group in their TSSE setup [50]. Moreover they report that their measurements seem to be depending on the contact pressure of the needles on the sample. This provides evidence of a different heat flow from the needles into the sample for different contact pressures. Assuming that the signals of Uchida et al. [7] originate from the ANE induced by the needles, one could imagine a temperature profile of their setup in which the needles are at a medium

temperature in comparison to the hot and the cold side of the sample. This would lead to a similar V_y dependence as observed by Uchida et al. [7]. However, this dependence should still be visible when removing the Pt strip, since the ANE is arising from the Py layer. Here Uchida et al. [7] see a vanishing signal excluding an ANE contribution. This circumstance shows that there is a strong need for detailed measurements for both electrical contact methods so that influences of the measuring technique to the TSSE can be excluded.

5.4 Influence of small misalignments

5.4.1 A finite out-of-plane magnetization

Our measurements are very sensitive to out-of-plane temperature gradients since these introduce the ANE to our in-plane measurement geometry. But also an out-of-plane magnetization with an in-plane temperature gradient leads to an ANE signal. In order to evaluate this contribution to our experiment we carefully check the alignment of the sample plane to the turning axis of the magnetic field and found a possible misalignment of 5° at maximum in both setups. In order to calculate the resulting maximum out-of-plane angle φ of the magnetization we start from the energy density $\frac{E}{V}$ including the demagnetization and Zeeman energy terms.

$$\frac{E}{V} = -0.5\mu_0 M_\mathrm{S}^2 \cos^2(\varphi) - \mu_0 M_\mathrm{S} H \cos(\varphi - \xi), \tag{5.3}$$

with $\mu_0 M_\mathrm{S} = 1\,\mathrm{T}$ the saturation magnetization of permalloy, H the external magnetic field, φ the angle of the magnetization with respect to the sample plane, and ξ the angle of $\vec{H}$ with respect to the sample plane. Including a maximum sweeping field $\mu_0 H$=5 mT and $\xi = 5°$ as the upper limit of misalignment we find for the equilibrium position of $\vec{M}$ an angle of $\varphi = 0.025°$. Taking the sample widths (bulk: 4 mm, membrane: 0.5 mm) and the typical temperature gradients (bulk: 3.6 K/mm, membrane: 240 K/mm) into account, this misalignment transforms to an ANE voltage of $V_\mathrm{y,misal.} = 16\,\mathrm{nV}$ for the bulk and $V_\mathrm{y,misal.} = 136\,\mathrm{nV}$ for the membrane samples. These values are the maximum transverse voltages which are expected for a misalignment of the magnetic field of 5° to the sample plane and measured directly on the Py layer. For samples with an attached detector strip this voltage will be reduced by some factor as mentioned in section 4.6. Since we only use the data points near ±5 mT to calculate the Δ signal, we can estimate the maximum contribution to Δ as $\max(\Delta_\mathrm{misal.}) \approx V_\mathrm{y,misal.}$. Now knowing the magnitude of the disturbance, we concentrate on the angular dependence of $\Delta_\mathrm{misal.}$. Here, as seen in Fig. 5.2, not only the tilt angle ξ of both planes

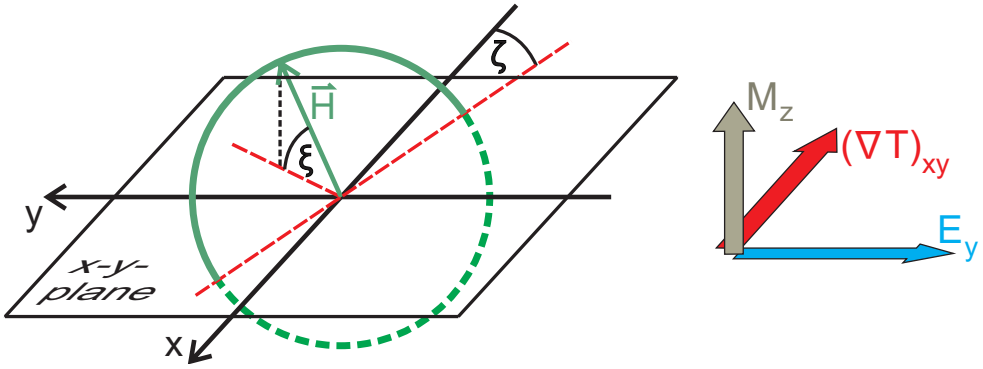

Figure 5.2: Sketch of misalignment between the rotation plane of the magnetic field (green) and the sample plane (grey shaded). The arrows on the right display the ANE originating from an out-of-plane magnetization M_z and an in-plane temperature gradient $(\vec{\nabla}T)_{xy}$.

but also the orientation ζ of the intersection line with respect to the x-axis needs to be regarded. For $\theta = \pm\zeta$ there is no out-of-plane field and $\Delta_{\text{misal.}} = 0$. For $\theta = \zeta \pm 90°$ the out-of-plane contribution is maximum and $\Delta_{\text{misal.}} = \mp V_{\text{y,misal.}}$. Complementing this to $\Delta_{\text{misal.}}(\theta)$ we get:

$$\Delta_{\text{misal.}}(\theta) = V_{\text{y,misal.}} \sin(\theta - \zeta) \tag{5.4}$$

But how can this $\Delta_{\text{misal.}}(\theta)$ influence our measurements in detail? $V_{\text{y,misal.}}$ is proportional to $(\vec{\nabla}T)_x$, it vanishes for $(\vec{\nabla}T)_x = 0$ and it does not depend on T_{strip}. Additionally, $V_{\text{y,misal.}}$ reverses sign for reversed $(\vec{\nabla}T)_x$. These properties make the misalignment of the field rotation axis a possible candidate for the vertical shift. In general, two cases have to be taken into account:
For $\zeta \approx 0°, 180°$ $\Delta_{\text{misal.}}(\theta)$ shows a phase shift in comparison to the original $\Delta(\theta)$ and thus is not influencing the $\Delta_0 \cos\theta$ fit and the extracted Δ_0 value.
For $\zeta \approx \pm 90°$ the $\Delta_0 \cos\theta$ fit function is summing up the original Δ_0 and $V_{\text{y,misal.}}$. As a worst case scenario ($\zeta \approx \pm 90°$ and $\xi = 5°$) we obtain a maximum contribution of 16 nV to the Δ_0 signal for $T_1 - T_2 = 50$ K in setup 1 and 136 nV in setup 2. For setup 1 this would mean that we get another contribution next to the AMTEP artifacts influencing the vertical shift of the Δ signal. When taking the short circuit effect of the Pt strip into account (see section 4.6), the maximum contribution reduces to about 8 nV which is inside the uncertainty of our measurement. Additionally, the calculations in section 4.8 show that the AMTEP artifacts can explain the measurements without the need for an additional $\Delta_{\text{misal.}}(\theta)$ contribution. Thus we do not expect any influence of a possible magnetic field misalignment in setup 1. For the suspended Py layers measured in setup 2 the maximum disturbance of a misalignment is 136 nV on a pure Py layer. By adding a Pt detector strip the magnitude will reduce by a factor of four

(see section 4.10) and is below the detection limit of setup 2. Thus, only for the measurements on pure Py it is possible to detect the effect of a misalignment. But since the AMTEP artifacts also describe this case very well we exclude a magnetic misalignment contribution in setup 2.

Nevertheless, it has to be mentioned that the whole measurement is very sensitive to the alignment of the sample and the magnetic field. By increasing the sweeping field to reduce the AMTEP artifacts one enhances $V_{\mathrm{y,misal.}}$. Especially in setup 1 care has to be taken when mounting the sample since the sample is glued along the x-direction between the two copper blocks. This geometry enhances the danger of a tilt along the y-axis ($\zeta = \pm 90°$) and a flat fit of the sample has to be checked.

5.4.2 A transverse temperature gradient

Another possible disturbance is the existence of a temperature gradient along the y-axis. This could be the case if there are irregularities in the connection to the heat sink. In the case of a finite $(\vec{\nabla}T)_y$ we get a second term in equation 2.32 for the AMTEP:

$$E_y = S_{yx} \cdot (\vec{\nabla}T)_x + S_{yy} \cdot (\vec{\nabla}T)_x \tag{5.5}$$

and taking the tensor from equation 2.29 this leads to an angular dependence

$$A(\theta) = A_0(S_\parallel - S_\perp)\left[(\vec{\nabla}T)_x \sin(2\theta) + (\vec{\nabla}T)_y \cos(2\theta)\right] - 0.5A_0(S_\parallel + S_\perp), \tag{5.6}$$

consistent with Pu et al. [65]. Thus a finite $(\vec{\nabla}T)_y$ leads to a shifted phase plus an additional offset in comparison to the $\sin\theta\cos\theta$ dependence for $(\vec{\nabla}T)_y = 0$. As an example, Meier et al. [56] observe a small phase shift in their study. In our measured data we do not observe any phase shift which is a proof for $(\vec{\nabla}T)_y << (\vec{\nabla}T)_x$. The influence of a small finite $(\vec{\nabla}T)_y$ to the ANE contribution ($\Delta(\theta)$) would also lead to a phase shift which is not observed.

5.5 The role of the phonons

The reduced phonon spectrum in the amorphous SiN_x membrane which acts as the substrate for the suspended Py layers in the study of Avery et al. [60] might be the reason for the vanishing TSSE in their measurements. In this work we

investigated both, suspended Py layers on SiN_x membranes, as well as Py layers on bulk substrates, to check this assumption. However, the missing TSSE in both cases does not give any further information about the role of the phonons in the substrate. The dilemma is that the TSSE in Py layers does not exist or is at least of non-measurable size. Thus, one cannot discuss about the role of the phonons for the TSSE since we do not observe any TSSE. Nevertheless, taking the ongoing discussion about the existence of the TSSE into account (including the possibility of the TSSE in insulators originating from the LSSE) the need to introduce the phonons as the mediating particle over distances longer than the spin diffusion length in the SSE theory does not exist anymore. This critical point should be taken into account in further theoretical models of the SSE.

6 Conclusion

6.1 Summary

After the first observation of the TSSE by the Saitoh group in Japan a debate on the existence of the TSSE in Py films came up. The main critical points are the missing reproducibility of their measurements and the possible misinterpretation of other magneto-thermoelectric effects. In this thesis, two types of samples are investigated: Thin Py layers on MgO and GaAs substrates and suspendend Py layers on SiN_x membranes. The measurements can be described by well known magneto-thermoelectric effects: The AMTEP and the ANE which limit the TSSE contribution to the noise level of our measurements of 10 nV. This is orders smaller than observed by Uchida et al. [7] in directly comparable measurements. In detail we observe the following contributions:

(1) AMTEP: The measured voltage signals are dominated by the AMTEP which is surprisingly not investigated by Uchida et al.. However, with its $\sin(\theta)\cos(\theta)$ symmetry this effect can be delimited from the TSSE.

(2) ANE: The ANE shares the $\cos(\theta)$ symmetry with the TSSE which makes it more difficult to separate both effects. However, the ANE is only present in the TSSE geometry in case of a finite out-of-plane temperature gradient. The measurements show that the amplitude of the $\cos(\theta)$ contribution (i.e. Δ_0) is still observable in case of a zero in-plane temperature gradient and thus cannot originate from the TSSE. The fact that Δ_0 scales with base temperature can be explained by a heat exchange via thermal radiation. FEM simulations support this statement.

(3) AMTEP artifact: After identifying the AMTEP and ANE contribution, a $\cos(\theta)$ feature of about 20 nV remains, which switches sign for opposite thermal gradient. This switch is a key feature of the TSSE. However, control measurements with Cu as a detector material and removed detector strip prove no link to the TSSE. Numerical calculations of the AMTEP reveal that a constant magnetic field, independent from the sweeping field, can generate an asymmetric contribution to the AMTEP. Here, the magnetic field of the earth is sufficient enough to explain the fine structure of Δ_0.

In summary, all measurements in this thesis can be explained by a sum of the above contributions. Additionally, the absence of the TSSE in both sample types implies a thinkover of the role of the phonons for the SSE in general.

The results in this thesis for Py layers give strong evidence of the absence of the TSSE in conducting FM in general. The next step is going to be the systematic investigation of the TSSE in semi conducting and isolating FM. Here, first preliminary results of other groups indicate the LSSE as a possible candidate to mime the TSSE contribution. Thus, further investigation of the TSSE is needed in order to clarify the existence of this effect.

Besides the discussion about the existence of the TSSE, its magnitude in conducting FM seems to be so small that an influence in future spintronic and spincaloritronic devices is negligible.

6.2 Personal view

In the last three years I had the possibility to participate in several workshops within the spincaloritronic community. There, the exchange with other PhD students working on the TSSE revealed the missing reproducibility of the TSSE. Even sample exchange programs revealed different results in different laboratories although the same sample was measured. Furthermore, I had the possibility to discuss with proponents of the TSSE like Ass.-Prof. Dr. Ken-ichi Uchida, Prof. Dr. Eiji Saitoh and Prof. Dr. Joseph Heremans as well as critics like Prof. Dr. Chia-Ling Chien and Ass.-Prof. Dr. Barry Zink. Including all this experience in my personal opinion the TSSE is not existing or at least below detectable quantity. Nevertheless, besides the TSSE the longitudinal configuration, the LSSE, seems to be more solid and could be reproduced many times in different materials. In general, this thesis solves a long time discussion about the existance of the TSSE at least in Py films and supports the importance of control measurements. Even if such „negative“ results may not be the award winning ones, new discoveries should be treated with constructive criticism and be checked carefully by the scientific community.

Bibliography

[1] G. Moore, "Cramming More Components Onto Integrated Circuits," *Proceedings of the IEEE*, vol. 86, no. 1, pp. 82–85, 1998.

[2] S. A. Wolf, D. D. Awschalom, R. A. Buhrman, J. M. Daughton, S. von Molnar, M. L. Roukes, A. Y. Chtchelkanova, and D. M. Treger, "Spintronics: A Spin-Based Electronics Vision for the Future," *Science*, vol. 294, no. 5546, pp. 1488–1495, 2001.

[3] G. E. W. Bauer, E. Saitoh, and B. J. van Wees, "Spin caloritronics," *Nature Materials*, vol. 11, pp. 391–399, 2012.

[4] J.-C. Le Breton, S. Sharma, H. Saito, S. Yuasa, and R. Jansen, "Thermal spin current from a ferromagnet to silicon by Seebeck spin tunnelling," *Nature*, vol. 475, pp. 82–85, 2011.

[5] A. Slachter, F. L. Bakker, J.-P. Adam, and B. J. van Wees, "Thermally driven spin injection from a ferromagnet into a non-magnetic metal," *Nature Physics*, vol. 6, pp. 879–882, 2010.

[6] M. Hatami, G. E. W. Bauer, Q. Zhang, and P. J. Kelly, "Thermal Spin-Transfer Torque in Magnetoelectronic Devices," *Phys. Rev. Lett.*, vol. 99, p. 066603, 2007.

[7] K. Uchida, S. Takahashi, K. Harii, J. Ieda, W. Koshibae, K. Ando, S. Maekawa, and E. Saitoh, "Observation of the spin Seebeck effect," *Nature*, vol. 455, pp. 778–781, 2008.

[8] J. Flipse, F. L. Bakker, A. Slachter, F. K. Dejene, and B. J. van Wees, "Direct observation of the spin-dependent Peltier effect," *Nature Nano.*, vol. 7, pp. 166–168, 2012.

[9] M. Dyakonov, "Spin Hall Effect," *arXiv*, p. arXiv:1210.3200, 2012.

[10] M. Dyakonov and V. Perel, "Current-induced spin orientation of electrons in semiconductors," *Physics Letters A*, vol. 35, no. 6, pp. 459 – 460, 1971.

[11] J. E. Hirsch, "Spin Hall Effect," *Phys. Rev. Lett.*, vol. 83, pp. 1834–1837, 1999.

[12] S. Zhang, "Spin Hall Effect in the Presence of Spin Diffusion," *Phys. Rev. Lett.*, vol. 85, pp. 393–396, 2000.

[13] H.-A. Engel, B. I. Halperin, and E. I. Rashba, "Theory of Spin Hall Conductivity in n-Doped GaAs," *Phys. Rev. Lett.*, vol. 95, p. 166605, 2005.

[14] N. Mott and H. Massey, "The Theory of Atomic Collisions," 1965.

[15] L. Berger, "Side-Jump Mechanism for the Hall Effect of Ferromagnets," *Phys. Rev. B*, vol. 2, pp. 4559–4566, 1970.

[16] J. Sinova, D. Culcer, Q. Niu, N. A. Sinitsyn, T. Jungwirth, and A. H. MacDonald, "Universal Intrinsic Spin Hall Effect," *Phys. Rev. Lett.*, vol. 92, p. 126603, 2004.

[17] S. Murakami, N. Nagaosa, and S.-C. Zhang, "Dissipationless Quantum Spin Current at Room Temperature," *Science*, vol. 301, no. 5638, pp. 1348–1351, 2003.

[18] Y. K. Kato, R. C. Myers, A. C. Gossard, and D. D. Awschalom, "Observation of the Spin Hall Effect in Semiconductors," *Science*, vol. 306, no. 5703, pp. 1910–1913, 2004.

[19] H. Zhao, E. J. Loren, H. M. van Driel, and A. L. Smirl, "Coherence Control of Hall Charge and Spin Currents," *Phys. Rev. Lett.*, vol. 96, p. 246601, 2006.

[20] J. Wunderlich, B. Kaestner, J. Sinova, and T. Jungwirth, "Experimental Observation of the Spin-Hall Effect in a Two-Dimensional Spin-Orbit Coupled Semiconductor System," *Phys. Rev. Lett.*, vol. 94, p. 047204, 2005.

[21] N. P. Stern, S. Ghosh, G. Xiang, M. Zhu, N. Samarth, and D. D. Awschalom, "Current-Induced Polarization and the Spin Hall Effect at Room Temperature," *Phys. Rev. Lett.*, vol. 97, p. 126603, 2006.

[22] T. Kimura, Y. Otani, T. Sato, S. Takahashi, and S. Maekawa, "Room-Temperature Reversible Spin Hall Effect," *Phys. Rev. Lett.*, vol. 98, p. 156601, 2007.

[23] E. Saitoh, M. Ueda, H. Miyajima, and G. Tatara, "Conversion of spin current into charge current at room temperature: Inverse spin-Hall effect," *Applied Physics Letters*, vol. 88, no. 18, p. 182509, 2006.

[24] L. Liu, T. Moriyama, D. C. Ralph, and R. A. Buhrman, "Spin-Torque Ferromagnetic Resonance Induced by the Spin Hall Effect," *Phys. Rev. Lett.*, vol. 106, p. 036601, 2011.

[25] Z. Feng, J. Hu, L. Sun, B. You, D. Wu, J. Du, W. Zhang, A. Hu, Y. Yang, D. M. Tang, B. S. Zhang, and H. F. Ding, "Spin Hall angle quantification from spin pumping and microwave photoresistance," *Phys. Rev. B*, vol. 85, p. 214423, 2012.

[26] A. Azevedo, L. H. Vilela-Leão, R. L. Rodríguez-Suárez, A. F. Lacerda Santos, and S. M. Rezende, "Spin pumping and anisotropic magnetoresistance voltages in magnetic bilayers: Theory and experiment," *Phys. Rev. B*, vol. 83, p. 144402, 2011.

[27] M. Obstbaum, M. Härtinger, H. G. Bauer, T. Meier, F. Swientek, C. H. Back, and G. Woltersdorf, "Inverse spin Hall effect in $Ni_{81}Fe_{19}$/normal-metal bilayers," *Phys. Rev. B*, vol. 89, p. 060407, 2014.

[28] K. Ando, S. Takahashi, K. Harii, K. Sasage, J. Ieda, S. Maekawa, and E. Saitoh, "Electric Manipulation of Spin Relaxation Using the Spin Hall Effect," *Phys. Rev. Lett.*, vol. 101, p. 036601, 2008.

[29] O. Mosendz, V. Vlaminck, J. E. Pearson, F. Y. Fradin, G. E. W. Bauer, S. D. Bader, and A. Hoffmann, "Detection and quantification of inverse spin Hall effect from spin pumping in permalloy/normal metal bilayers," *Phys. Rev. B*, vol. 82, p. 214403, 2010.

[30] E. H. Hall, "On a New Action of the Magnet on Electric Currents," *American Journal of Mathematics*, vol. 2, no. 3, pp. pp. 287–292, 1879.

[31] A. v. Ettingshausen and W. Nernst, "Über das Auftreten electromotorischer Kräfte in Metallplatten, welche von einem Wärmestrome durchflossen werden und sich im magnetischen Felde befinden," *Annalen der Physik*, vol. 265, no. 10, pp. 343–347, 1886.

[32] S. Onoda, N. Sugimoto, and N. Nagaosa, "Intrinsic Versus Extrinsic Anomalous Hall Effect in Ferromagnets," *Phys. Rev. Lett.*, vol. 97, p. 126602, 2006.

[33] N. Nagaosa, J. Sinova, S. Onoda, A. H. MacDonald, and N. P. Ong, "Anomalous Hall effect," *arXiv*, p. arXiv:0904.4154, 2009.

[34] T. Miyasato, N. Abe, T. Fujii, A. Asamitsu, S. Onoda, Y. Onose, N. Nagaosa, and Y. Tokura, "Crossover Behavior of the Anomalous Hall Effect and Anomalous Nernst Effect in Itinerant Ferromagnets," *Phys. Rev. Lett.*, vol. 99, p. 086602, 2007.

[35] W. Thomson, "On the Electro-Dynamic Qualities of Metals: Effects of Magnetization on the Electric Conductivity of Nickel and of Iron," *Proceedings of the Royal Society of London*, vol. 8, pp. 546–550, 1856.

[36] V. D. Ky, "Planar Hall Effect in Ferromagnetic Films," *physica status solidi (b)*, vol. 26, no. 2, pp. 565–569, 1968.

[37] V. D. Ky, "Planar Hall and Nernst Effect in Ferromagnetic Metals," *physica status solidi (b)*, vol. 22, no. 2, pp. 729–736, 1967.

[38] K. Uchida, T. Ota, K. Harii, K. Ando, H. Nakayama, and E. Saitoh, "Electric detection of the spin-Seebeck effect in ferromagnetic metals (invited)," *Journal of Applied Physics*, vol. 107, no. 9, p. 09A951, 2010.

[39] K. Uchida, J. Xiao, H. Adachi, J. Ohe, S. Takahashi, J. Ieda, T. Ota, Y. Kajiwara, H. Umezawa, H. Kawai, G. E. W. Bauer, S. Maekawa, and E. Saitoh, "Spin Seebeck insulator," *Nature Materials*, vol. 9, pp. 894–897, 2010.

[40] C. M. Jaworski, J. Yang, S. Mack, D. D. Awschalom, J. P. Heremans, and R. C. Myers, "Observation of the spin-Seebeck effect in a ferromagnetic semiconductor," *Nature Materials*, vol. 9, pp. 898–903, 2010.

[41] D. Meier, T. Kuschel, L. Shen, A. Gupta, T. Kikkawa, K. Uchida, E. Saitoh, J.-M. Schmalhorst, and G. Reiss, "Thermally driven spin and charge currents in thin $NiFe_2O_4$/Pt films," *Phys. Rev. B*, vol. 87, p. 054421, 2013.

[42] K. Uchida, T. Nonaka, T. Kikkawa, Y. Kajiwara, and E. Saitoh, "Longitudinal spin Seebeck effect in various garnet ferrites," *Phys. Rev. B*, vol. 87, p. 104412, 2013.

[43] K. Uchida, H. Adachi, T. Ota, H. Nakayama, S. Maekawa, and E. Saitoh, "Observation of longitudinal spin-Seebeck effect in magnetic insulators," *Applied Physics Letters*, vol. 97, no. 17, p. 172505, 2010.

[44] G. Siegel, M. C. Prestgard, S. Teng, and A. Tiwari, "Robust longitudinal spin-Seebeck effect in Bi-YIG thin films," *Sci. Rep.*, vol. 4, p. 4429, 2014.

[45] S. Y. Huang, W. G. Wang, S. F. Lee, J. Kwo, and C. L. Chien, "Intrinsic Spin-Dependent Thermal Transport," *Phys. Rev. Lett.*, vol. 107, p. 216604, 2011.

[46] J. Xiao, G. E. W. Bauer, K. Uchida, E. Saitoh, and S. Maekawa, "Theory of magnon-driven spin Seebeck effect," *Phys. Rev. B*, vol. 81, p. 214418, 2010.

[47] H. Adachi, K.-i. Uchida, E. Saitoh, J.-i. Ohe, S. Takahashi, and S. Maekawa, "Gigantic enhancement of spin Seebeck effect by phonon drag," *Applied Physics Letters*, vol. 97, no. 25, p. 252506, 2010.

[48] C. M. Jaworski, J. Yang, S. Mack, D. D. Awschalom, R. C. Myers, and J. P. Heremans, "Spin-Seebeck Effect: A Phonon Driven Spin Distribution," *Phys. Rev. Lett.*, vol. 106, p. 186601, 2011.

[49] K. Uchida, H. Adachi, T. An, T. Ota, M. Toda, B. Hillebrands, S. Maekawa, and E. Saitoh, "Long range spin Seebeck effect and acoustic spin pumping," *Nature Materials*, vol. 10, pp. 737–741, 2011.

[50] P. G. Reiss, "private communication," *University of Bielefeld*, 2013.

[51] M. Althammer, S. Meyer, H. Nakayama, M. Schreier, S. Altmannshofer, M. Weiler, H. Huebl, S. Gepraegs, M. Opel, R. Gross, D. Meier, C. Klewe, T. Kuschel, J.-M. Schmalhorst, G. Reiss, L. Shen, A. Gupta, Y.-T. Chen, G. E. W. Bauer, E. Saitoh, and S. T. B. Goennenwein, "Quantitative study of the spin Hall magnetoresistance in ferromagnetic insulator/normal metal hybrids," *Phys. Rev. B*, vol. 87, p. 224401, 2013.

[52] Y. M. Lu, Y. Choi, C. M. Ortega, X. M. Cheng, J. W. Cai, S. Y. Huang, L. Sun, and C. L. Chien, "Pt Magnetic Polarization on $Y_3Fe_5O_{12}$ and Magnetotransport Characteristics," *Phys. Rev. Lett.*, vol. 110, p. 147207, 2013.

[53] M. Schreier, A. Kamra, M. Weiler, J. Xiao, G. E. W. Bauer, R. Gross, and S. T. B. Goennenwein, "Magnon, phonon, and electron temperature profiles and the spin Seebeck effect in magnetic insulator/normal metal hybrid structures," *Phys. Rev. B*, vol. 88, p. 094410, 2013.

[54] S. Chikazumi, "Study of Magnetic Annealing on Ni3Fe Single Crystal," *Journal of the Physical Society of Japan*, vol. 11, no. 5, pp. 551–558, 1956.

[55] J. F. Dillinger and R. M. Bozorth, "Heat Treatment of Magnetic Materials in a Magnetic Field I. Survey of Iron-Cobalt-Nickel Alloys," *Journal of Applied Physics*, vol. 6, no. 9, pp. 279–284, 1935.

[56] D. Meier, D. Reinhardt, M. Schmid, C. H. Back, J.-M. Schmalhorst, T. Kuschel, and G. Reiss, "Influence of heat flow directions on Nernst effects in Py/Pt bilayers," *Phys. Rev. B*, vol. 88, p. 184425, 2013.

[57] V. D. Ky, "The Planar Nernst Effect in Permalloy Films," *physica status solidi (b)*, vol. 17, no. 2, pp. K207–K209, 1966.

[58] T. Kimura, J. Hamrle, and Y. Otani, "Estimation of spin-diffusion length from the magnitude of spin-current absorption: Multiterminal ferromagnetic/nonferromagnetic hybrid structures," *Phys. Rev. B*, vol. 72, p. 014461, 2005.

[59] F. J. Jedema, A. T. Filip, and B. J. van Wees, "Electrical spin injection and accumulation at room temperature in an all-metal mesoscopic spin valve," *Nature*, vol. 410, pp. 345–348, 2001.

[60] A. D. Avery, M. R. Pufall, and B. L. Zink, "Observation of the Planar Nernst Effect in Permalloy and Nickel Thin Films with In-Plane Thermal Gradients," *Phys. Rev. Lett.*, vol. 109, p. 196602, 2012.

[61] R. Urban, G. Woltersdorf, and B. Heinrich, "Gilbert Damping in Single and Multilayer Ultrathin Films: Role of Interfaces in Nonlocal Spin Dynamics," *Phys. Rev. Lett.*, vol. 87, p. 217204, 2001.

[62] B. Heinrich, Y. Tserkovnyak, G. Woltersdorf, A. Brataas, R. Urban, and G. E. W. Bauer, "Dynamic Exchange Coupling in Magnetic Bilayers," *Phys. Rev. Lett.*, vol. 90, p. 187601, 2003.

[63] S. Mizukami, Y. Ando, and T. Miyazaki, "Ferromagnetic resonance linewidth for NM/80NiFe/NM films (NM=Cu, Ta, Pd and Pt)," *Journal of Magnetism and Magnetic Materials*, vol. 226-230, no. 0, pp. 1640–1642, 2001. Proceedings of the International Conference on Magnetism (ICM 2000).

[64] F. D. Czeschka, L. Dreher, M. S. Brandt, M. Weiler, M. Althammer, I.-M. Imort, G. Reiss, A. Thomas, W. Schoch, W. Limmer, H. Huebl, R. Gross, and S. T. B. Goennenwein, "Scaling Behavior of the Spin Pumping Effect in Ferromagnet-Platinum Bilayers," *Phys. Rev. Lett.*, vol. 107, p. 046601, 2011.

[65] Y. Pu, E. Johnston-Halperin, D. D. Awschalom, and J. Shi, "Anisotropic Thermopower and Planar Nernst Effect in $Ga_{1-x}Mn_xAs$ Ferromagnetic Semiconductors," *Phys. Rev. Lett.*, vol. 97, p. 036601, 2006.

Index of abbreviations

AHE	Anomalous Hall Effect
ALD	Atomic Layer Deposition
AMR	Anisotropic Magneto Resistance
AMTEP	Anisotropic Magneto-ThermoElectric Power
ANE	Anomalous Nernst Effect
CPU	Central Process Unit
FEM	Finite Element Model
FIB	Focused Ion Beam
FM	FerroMagnet
ISHE	Inverse Spin Hall Effect
LSSE	Longitudinal Spin Seebeck Effect
NM	Normal Metal
RAM	Random Access Memory
RT	Room Temperature
SEM	Scanning Electron Microscope
SHE	Spin Hall Effect
SOI	Spin Orbit Interaction
SSE	Spin Seebeck effect
STT	Spin Transfer Torque
TMR	Tunneling Magneto Resistance
TPD	Thermal Design Power
TSSE	Transverse Spin Seebeck effect

List of publications

• The systematic study of the TSSE in Py thin films in this thesis is published as:

„**Transverse Spin Seebeck Effect versus Anomalous and Planar Nernst Effects in Permalloy Thin Films**“ M. Schmid, S. Srichandan, D. Meier, T. Kuschel, J.-M. Schmalhorst, M. Vogel, G. Reiss, C. Strunk, and C. H. Back, Physical Review Letters **111**, 187201 (2013)

• In collaboration with the work group of Prof. Dr. Günther Reiss a study of TSSE measurements utilizing measuring tips is published as:

„**Influence of heat flow directions on Nernst effects in Py/Pt bilayers**“ D. Meier, D. Reinhardt, M. Schmid, C. H. Back, J.-M. Schmalhorst, T. Kuschel and G. Reiss, Physical Review B **88**, 184425 (2013)

• Further investigations on the LSSE in the transverse configuration will be published as:

„**Contribution of a longitudinal spin Seebeck effect in transverse spin Seebeck effect experiments in Pt/YIG and Pt/NFO**“ D. Meier, D. Reinhardt, M. van Straaten, C. Klewe, M. Althammer, S.T.B. Gönnenwein, A. Gupta, M. Schmid, C. H. Back, J.-M. Schmalhorst, T. Kuschel and G. Reiss, to be published

• During the first year of my PhD, I took on the work of my diploma thesis concerning hot electron transport. The final results of this work are published as:

„**Antiferromagnetic coupling across silicon regulated by tunneling currents**“ R. R. Gareev, M. Schmid, J. Vancea, C. H. Back, R. Schreiber, D. Bürgler, C. M. Schneider, F. Stromberg and H. Wende, Applied Physics Letters **100** 022406 (2012)

• Furthermore, I participated in the discovery of the spin solar cell which is published as:

„**Demonstration of the spin solar cell and spin photodiode effect**“ B. Endres, M. Ciorga, M. Schmid, M. Utz, D. Bougeard, D. Weiss, G. Bayreuther and C.H. Back, Nature Communications **4**, 2068 (2013)

Danksagung

Zu Beginn möchte ich Prof. Dr. Christian Back für das außerordentlich interessante Thema aus dem Bereich der Spin-Caloritronic danken. Ich schätzte vor allem die Freiheit, meine eigenen Ideen durchführen und Neues ausprobieren zu können. Danke auch für die konstruktiven Ideen im Laufe meiner Arbeit und für die fruchtbaren Diskussionen, die zum besseren Verständnis beigetragen haben.

Prof. Dr. Günther Reiss möchte ich für die freundliche Unterstützung danken. Der informative Austausch zwischen Bielefeld und Regensburg hat mir sehr geholfen. In diesem Zusammenhang danke ich auch Martin Schmalhorst, Timo Kuschel und Daniel Meier für ihre Hilfe und die anregenden Diskussionen.

Auch Prof. Dr. Christoph Strunk danke ich für die bereichernden Erläuterungen.

Besonderer Dank gilt Sasmita Srichandan für die Zusammenarbeit und die Herstellung sowie Vermessung der Membran-Proben.

Ein großer Dank gilt auch Anatoly Shestakov für die systematischen numerischen Berechnungen und Unterstützung bei den Messungen. Ich wünsche ihm ein erfolgreiches Weiterführen dieser Arbeit.

Martin Obstbaum, Markus Härtinger und Martin Decker danke ich für ihre anschaulichen Erklärungen in den Bereichen Spinpumpen und des Spin Hall Effekts.

Dank gilt auch Michael Vogel für die gelungenen COMSOL Simulationen, die die gewonnenen Ergebnisse in dieser Arbeit unterstützen.

Martin Buchner möchte ich für die anregenden Diskussionen und die konstruktive Kritik an dieser Arbeit danken.

Bernhard Endres danke ich für die kompetente Unterstützung bei der Interpretation der ersten Messergebnisse.

Auch meinen Bürokollegen gilt besonderer Dank für die angenehme Arbeitsatmosphäre.

Für die Unterstützung beim Aufbau der Messapparaturen möchte ich mich beim Team der mechanischen sowie der elektronischen Werkstatt Physik, die mir mit Rat und Tat zur Seite standen, bedanken.

Zuletzt bedanke ich mich bei allen Kollegen am Lehrstuhl Back, generell für die freundliche Atmosphäre aber auch für die selbstlose Hilfe bei vielen Kleinigkeiten.